

A study of extreme C III]1908 & [O III]88/[C II]157 emission in Pox 186: implications for JWST+ALMA (FUV+FIR) studies of distant galaxies

Nimisha Kumari¹*, Renske Smit², Claus Leitherer³, Joris Witstok^{4,5}, Mike J Irwin⁶,

Marco Sirianni⁷, Alessandra Aloisi³

¹AURA for European Space Agency (ESA), ESA Office, Space Telescope Science Institute, 3700 San Martin Drive, Baltimore, MD, 21218, USA

²Astrophysics Research Institute, Liverpool John Moores University, Liverpool, L35 UG, UK

³Space Telescope Science Institute, Baltimore, MD, 21218, USA

⁴Kavli Institute for Cosmology, University of Cambridge, Madingley Road, Cambridge CB3 0HA, UK

⁵Cavendish Laboratory, University of Cambridge, 19 JJ Thomson Avenue, Cambridge CB3 0HE, UK

⁶Institute of Astronomy, University of Cambridge, Madingley Road, Cambridge CB3 0HA, UK

⁷European Space Agency (ESA), ESA Office, Space Telescope Insitute, 3700 San Martin Drive, Baltimore, MD 21218, USA

Accepted XXX. Received YYY; in original form ZZZ

ABSTRACT

Carbon spectral features are ubiquitous in the ultraviolet (UV) and far-infrared (FIR) spectra of galaxies in the epoch of reionization (EoR). We probe the ionized carbon content of a blue compact dwarf galaxy Pox 186 using the UV, optical, mid-infrared and FIR data taken with telescopes in space (Hubble, Spitzer, Herschel) and on the ground (Gemini). This local ($z \sim 0.0040705$) galaxy is likely an analogue of EoR galaxies, as revealed by its extreme FIR emission line ratio, $[\text{O III}]88 \mu\text{m}/[\text{C II}]157 \mu\text{m} (>10)$. The UV spectra reveal extreme C III] $\lambda\lambda$ 1907, 1909 emission with the strongest equivalent width (EW) = $35.85 \pm 0.73 \text{ \AA}$ detected so far in the local ($z \sim 0$) Universe, a relatively strong C IV] $\lambda\lambda$ 1548, 1550 emission with EW = $7.95 \pm 0.45 \text{ \AA}$, but no He II] λ 1640 detection. Several scenarios are explored to explain the high EW of carbon lines, including high effective temperature, high carbon-to-oxygen ratio, slope and upper mass of top-heavy initial mass function, hard ionizing radiation and in-homogeneous dust distribution. Both C III] and C IV] line profiles are broadened with respect to the O III] λ 1660 emission line. Each emission line of C IV] $\lambda\lambda$ 1548, 1550 shows the most distinct double-peak structure ever detected which we model via two scenarios, firstly a double-peaked profile that might emerge from resonant scattering and secondly a single nebular emission line along with a weaker interstellar absorption. The study demonstrates that galaxies with extreme FIR emission line ratio may also show extreme UV properties, hence paving a promising avenue of using FIR+UV in the local (via HST+Herschel/SOFIA) and distant (via JWST+ALMA) Universe for unveiling the mysteries of the EoR.

Key words: galaxies:dwarfs – galaxies:abundances – galaxies:high-redshift

1 INTRODUCTION

Understanding the reionization of the Universe is one of the frontier goals of modern astronomy. Several theoretical and observational efforts have been made to answer the related pressing questions such as when and how first galaxies formed (e.g., Stark 2016) and whether these first galaxies reionized the intergalactic medium (IGM; e.g., Robertson et al. 2010). A first step to answer these questions is to search for the early galaxies in the epoch of reionization (EoR) and characterize their properties.

Deep imaging campaigns have been quite successful in searching for such sources. For example, the Hubble Space Telescope (HST) allowed us to compile large samples of early galaxies via deep near-infrared (NIR) imaging programs such as the Great Observatories Origins Deep Survey (GOODS, Giavalisco et al. 2004), Extreme Deep Field (XDF, Illingworth et al. 2013) and Cosmic Assembl Near-Infrared Deep Extragalactic Legacy Survey (CANDELS, Gro-

gin et al. 2011; Koekemoer et al. 2011). However, spectroscopy is essential to characterize the properties of these sources. Until the launch of the James Webb Space Telescope (JWST), the rest-frame ultraviolet (UV) spectroscopy was available for only a few EoR galaxies (e.g., Sobral et al. 2015; Stark et al. 2017; Topping et al. 2021; Hutchison et al. 2019). The JWST observations are significantly improving the dearth of UV spectroscopy for the EoR galaxies via the planned follow-up spectroscopic surveys of the Hubble deep fields (Robertson 2021; Curtis-Lake et al. 2022; Bunker et al. 2023). Similarly, the exquisite sensitivity of the Atacama Large Millimeter Array (ALMA) has made it possible to obtain the far-infrared (FIR) spectroscopy of EoR galaxies (e.g., Maiolino et al. 2015; Carniani et al. 2017; Smit et al. 2018; Bouwens et al. 2022; Witstok et al. 2022). The combined JWST+ALMA spectroscopic observations will significantly enhance our understanding of the EoR.

An indirect approach to probe the nature of reionization sources while efficiently using the two simultaneously-operating state-of-the-art facilities, JWST and ALMA, is to perform detailed studies of the physical processes operating in local galaxies which might resemble

* E-mail: kumari@stsci.edu

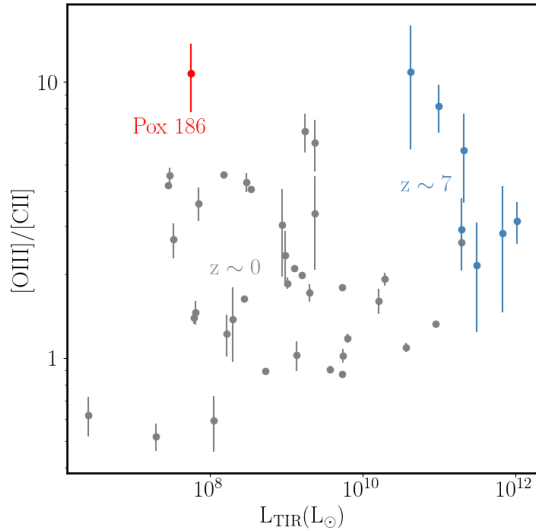


Figure 1. $[\text{O III}] 88 \mu\text{m}/[\text{C II}] 157 \mu\text{m}$ line ratio versus IR luminosity for Pox 186 (red point), galaxies at $z=7$ (blue points, Hashimoto et al. 2019; Witstok et al. 2022; Ren et al. 2023) and local dwarf galaxies (grey points, Cormier et al. 2015).

EoR galaxies. Several different criteria have been devised so far to identify the local analogues of high-redshift galaxies, including gas-phase metallicity, star-formation rate, compactness, stellar mass, UV luminosity, dust attenuation, $\text{Ly}\alpha$ emission, colour, and ionization state among many others. Some established classes of local analogues of high-redshift galaxies are blue compact dwarf galaxies (BCD, Searle & Sargent 1972), green peas (GP, Cardamone et al. 2009) and blueberries (Yang et al. 2017), though it is not clear whether these galaxy populations also resemble the EoR galaxies, mainly because of the dearth of data available on EoR galaxies so far.

One of the goals of this paper is to demonstrate the use of FIR line ratio $[\text{O III}] 88 \mu\text{m}/[\text{C II}] 157 \mu\text{m}$ for identifying the local analogues of the EoR galaxies. $[\text{O III}] 88 \mu\text{m}$ originate from the ionized gas, $[\text{C II}] 157 \mu\text{m}$ may originate from both the ionized as well as neutral interstellar medium (ISM), and their relative strengths (i.e. $[\text{O III}] 88 \mu\text{m}/[\text{C II}] 157 \mu\text{m}$ line ratio) can potentially tell us about the porosity of ISM (Chevance et al. 2016; Polles et al. 2019). The ALMA observations of EoR galaxies (Figure 1, blue points) reveal that $[\text{O III}] 88 \mu\text{m}/[\text{C II}] 157 \mu\text{m}$ line ratio may vary in the range 1–10, indicating a highly porous ISM which will facilitate the leakage of ionizing photons required for reionization of the neutral IGM. The Herschel Dwarf Galaxies Survey (Madden et al. 2013; Cormier et al. 2015) reveal a large population of local dwarf galaxies with $[\text{O III}] 88 \mu\text{m}/[\text{C II}] 157 \mu\text{m} > 1$ (Figure 1, grey points), which are potentially the local analogues of EoR galaxies.

In an attempt to explore and establish using $[\text{O III}] 88 \mu\text{m}/[\text{C II}] 157 \mu\text{m}$ as a criterion for identifying the EoR local analogues, we obtained HST UV and spatially-resolved optical spectroscopy of Pox 186, a unique dwarf galaxy showing the highest $[\text{O III}] 88 \mu\text{m}/[\text{C II}] 157 \mu\text{m}$ ever detected in the local Universe (Figure 1, red point). Moreover, Ramambason et al. (2022) shows that this galaxy has an ionizing photon escape fraction of $\sim 40\%$, thus making it ideal for this study. Pox 186 was originally discovered in Kunth et al. (1981), and was thought to be a protogalaxy. Corbin & Vacca (2002) later shows that Pox 186

is an ultra-compact galaxy still in the process of formation with a majority of star-formation concentrated in the central star cluster of mass $10^5 M_{\odot}$. Figure 2 shows a narrow-band optical image of Pox 186 taken with Wide Field Planetary Camera2 onboard HST, along with the field-of-view (FOV) of instruments of primary observations used in this work. Table 1 lists some of the main physical properties of Pox 186, along with information about the UV and optical observing strategy. A typical UV spectrum of star-forming galaxies is known to show prominent spectral features such as $\text{Ly}\alpha\lambda 1215$, $\text{C IV}\lambda\lambda 1548, 1550$, $\text{He II}\lambda 1640$, $\text{O III}\lambda\lambda 1660, 1666$, $[\text{C III}]\lambda 1907$ and $\text{C III}\lambda 1909$ ¹, which have been used to infer information regarding hardness of radiation fields, ionization conditions, metal-content, wind properties within galaxies at all redshifts (e.g., Shapley et al. 2003; Senchyna et al. 2017; Nakajima et al. 2018; Schmidt et al. 2021). In this paper, we mainly focus on the ionized carbon spectral features, $\text{C IV}\lambda\lambda 1548, 1550$ and $\text{C III}\lambda\lambda 1907, 1909$, however, we complement the UV analysis with the spatially-resolved optical, mid-infrared (MIR) and FIR data.

The paper is organized as follows: Section 2 presents an overview of the data used in this work, including UV, optical, MIR and FIR. For UV and optical data, we explain the initial data reduction and processing. The MIR and FIR data are archival. In Section 3, we present the results of the multi-wavelength data analysis which includes the estimates of redshift, distance, flux and equivalent widths of detected emission lines and reddening. We also determine several physical properties of the ionized gas and the ionizing stellar population, such as electron temperature and density, gas-phase metallicity, ionization parameters, effective temperature and softness parameters. Section 4 presents a discussion focusing on UV carbon features including their large equivalent widths, line profiles and relative chemical abundance. We also discuss the implication of this study on future JWST+ALMA studies of reionization-era galaxies. Section 5 summarizes our main results.

In the rest of the paper, we assume a flat Λ CDM cosmology with $H_0 = 70 \text{ km s}^{-1} \text{ Mpc}^{-1}$, $\Omega_m = 0.3$. The gas-phase solar metallicity is assumed to be $12 + \log(\text{O}/\text{H})_{\odot} = 8.69$ (Asplund et al. 2009).

2 OBSERVATIONS

2.1 HST/UV spectroscopy

The HST/COS observations were taken as part of the General Observing programs in HST Cycles 27 and 28 (GO: 16071 and 16445, PI: N Kumari) at lifetime adjustment position 4 (LP=4). Before taking each UV spectrum, the NUV target acquisition image is taken using the Mirror A. The FUV and NUV spectra were taken with the 2.5 arcsec diameter Primary Science Aperture (PSA) using the medium resolution gratings, G130M, G160M and G185M centred at 1291\AA , 1623\AA and 1913\AA , respectively. We used all FP-POS positions for better spectral sampling and increased signal-to-noise (S/N). Table 1 lists the exposure times for gratings and Mirror A used within the two HST programs. All HST/COS data were processed with the standard data reduction pipeline CALCOS version 3.4.0.

Figure A1 shows the HST/COS NUV target acquisition image

¹ In the rest of the paper, we will refer the two carbon emission lines $[\text{C III}]\lambda 1907$ and $\text{C III}\lambda 1909$ as $\text{C III}\lambda\lambda 1907, 1909$, which is a popular notation in literature.

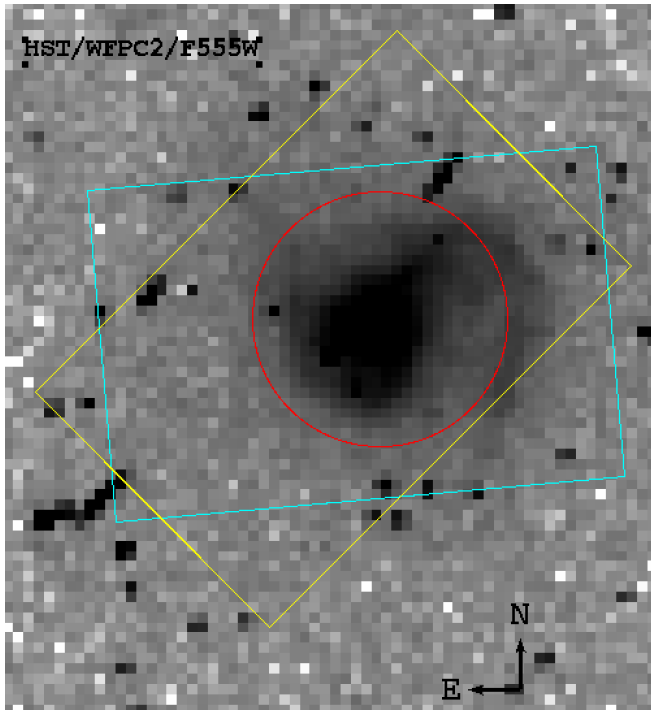


Figure 2. HST/WFPC2 image of Pox 186 taken in F555W filter (Prog id: 8333) on which we overlay FOVs of all primary observations used in this work. The red circle denotes the HST/COS aperture of $1.25''$ radius (PIDs: 16445, 16071). The yellow and cyan rectangles of size $3.5'' \times 5''$ denote the FOVs of GMOS-N IFU programs GN-2020A-FT-105 and GN-2021A-FT-111, respectively.

where the red circle denotes the 2.5 arcsec COS spectroscopic aperture. The wavelength settings allow us to cover several spectral features consisting of ISM (red), photospheric (purple), wind (yellow) and nebular (brown) lines as shown in Figures 3a and 3b.

2.2 GMOS-N optical spectroscopy

We obtained the spatially-resolved optical spectroscopy of Pox 186 using the GMOS (Hook et al. 2004) and IFU (GMOS-N IFU; Allington-Smith et al. 2002) at Gemini-North telescope in Hawaii, as part of two separate programs (PID: GN-2020A-FT-105, GN-2021A-FT-111, PI: N Kumari). The first program focussed on covering the optical wavelength range of $\sim 3500\text{--}8000\text{\AA}$, while the second program allowed us to cover the near-infrared (NIR) wavelength range of $\sim 8000\text{--}10000\text{\AA}$. The observations were taken in one-slit queue mode providing FOV of $3.5'' \times 5''$, large enough to cover the entire galaxy (Figure 2). Along with the science exposures, standard calibration observations were obtained including GCAL flats, CuAr lamp for wavelength calibration and standard star HZ44 for flux calibration.

We performed the basic steps of data reduction using the standard GEMINI reduction pipeline (version v1.15) written in Image Reduction and Analysis Facility (IRAF, version v2.16)². These basic steps included bias subtraction, flat field correction, wavelength

² IRAF is distributed by the National Optical Astronomy Observatory, which is operated by the Association of Universities for Research in Astronomy (AURA) under a cooperative agreement with the National Science Foundation.

Table 1. Basic data and HST/COS exposure times for Pox 186

Pox 186		
Morphological type	BCD	
RA (J2000)	13 25 48.641	
Dec (J2000)	-11 36 37.94	
Redshift ^a	0.0040705	
Distance (Mpc) ^a	17.5	
V (mag) ^b	17.43 ± 0.03	
B (mag) ^b	17.93 ± 0.53	
M_{HI} (M_{\odot}) ^c	$< 16.1 \times 10^5$	
COS Setting	Central wavelength (\AA)	Exposure time (s)
G130M ^d	1291	5123.36
G160M ^e	1623	4528.064
G185M ^e	1913	13428.864
Mirror A	–	7×3^f
GMOS gratings	Central wavelength (\AA)	Exposure time (s)
B600+_G5307 ^g	4650	870×3
B600+_G5307 ^g	4700	870×3
R831+_G5302 ^g	6900	950×2
R831+_G5302 ^g	6950	950×3
R831+_G5302 ^h	8800	1000×3
R831+_G5302 ^h	8900	1000×4

Notes: ^a: This work; ^b: Guseva et al. (2004); ^c: Begum & Chengalur (2005); ^d: HST/COS PID 16445; ^e: HST/COS PID 16071; ^f: Target acquisition was done thrice using Mirror A, every time before taking COS/FUV and COS/NUV spectra; ^g: GMOS PID:GN-2020A-FT-105; ^h: GMOS PID: GN-2021A-FT-111.

Table 2. IR emission line fluxes of Pox 186 from Cormier et al. (2015).

Emission lines	Observed Fluxes
[S IV] 10.5 μm	36.29 ± 3.66
[Ne II] 12.8 μm	0.95 ± 0.25
[Ne III] 15.6 μm	13.81 ± 3.33
[S III] 18.7 μm	7.37 ± 1.25
[O III] 88 μm	33.70 ± 3.33
[C II] 157 μm	3.14 ± 0.81

Notes: Fluxes are in $10^{-18} \text{ W m}^{-2}$.

calibration, sky subtraction, and differential atmospheric correction finally producing the 3D data cubes, and have been described in detail in Kumari (2018). New GMOS-N detectors were installed in 2017, which further required the quantum efficiency correction for all flats. We also used the L.A.Cosmic (van Dokkum 2001) to remove the cosmic rays from the science exposures. We chose a spatial sampling of $0.25''$ for the final three-dimensional data cubes. We thus obtain three three-dimensional data cubes. We scale the flux of each of the three cubes using the methodology described in Appendix B.

2.3 Ancillary Mid-Infrared and Far-Infrared spectroscopy

MIR: Pox 186 was observed with the Spitzer telescope in the low-resolution ($R \approx 60\text{--}127$) mode using long-slits of the InfraRed Spectrograph in the (IRS; Houck et al. 2004). The width of long slit is $\sim 3.6''$, and its point-spread function (PSF) may extend beyond the

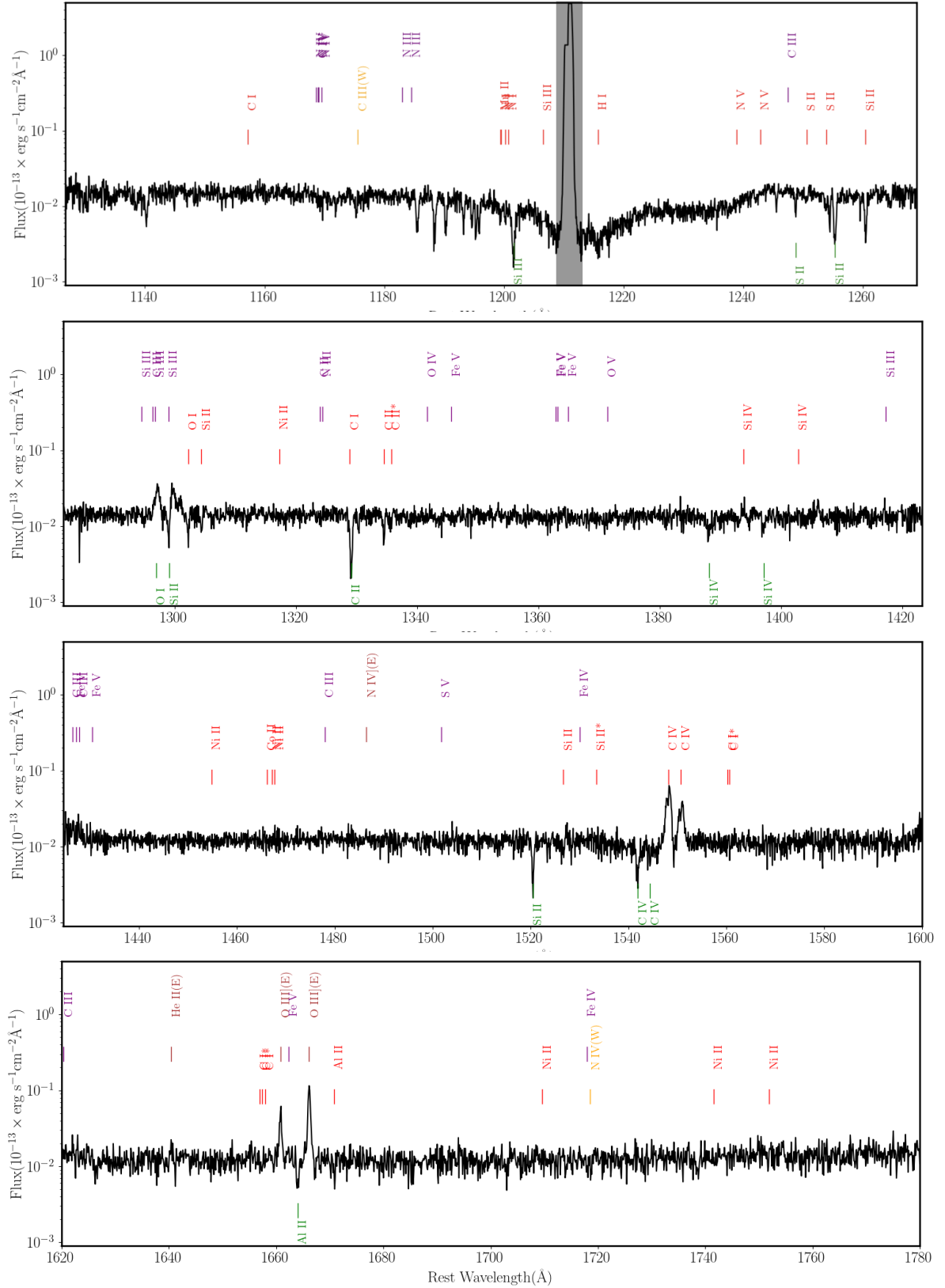


Figure 3a. HST/COS FUV spectra of Pox 186 taken with G130M/1291 (upper two panels) and G160M/1623 (lower two panels). These fluxes are smoothed by a boxcar filter of 6 pixels for better visualization. These spectra show several spectral features consisting of ISM (red), photospheric (purple), wind (yellow) and nebular (brown) lines. The milky way lines are marked in green. Note that not all marked lines are detected, and are provided here for reference. The geocoronal emission is marked by a grey shaded region in the first panel.

Table 3. Emission line redshift determinations

Emission lines	λ_{Rest} (Å)	λ_{Obs} (Å)	z
O III] λ 1660	1660.81	1667.6	0.004086
O III] λ 1666	1666.15	1672.95	0.004079
C III] λ 1907	1906.68	1914.43	0.004066
C III] λ 1909	1908.73	1916.46	0.004051

z (Mean \pm Std)^a 0.0040705 \pm 0.000013

Notes: Mean and Std denote the mean and standard deviations of the redshifts estimated from the emission lines.

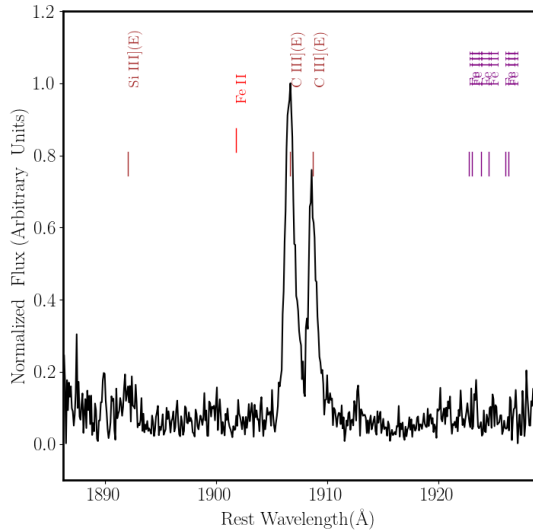


Figure 3b. HST/COS FUV spectra of Pox 186 taken with G185M/1913. These fluxes are smoothed by a boxcar filter of 2 pixels for better visualization. Note that the shown spectrum only represents the middle segment of the G185M/1913 grating, and the other two segments do not show any spectral feature.

slit width. Cormier et al. (2015) reports the MIR emission line fluxes after taking into account PSF.

FIR: Pox 186 was also observed with Herschel using the PACS which covers a total FOV of $47'' \times 47''$ and has a beam size of $9''$ and $12''$ at $60 \mu\text{m}$ and $160 \mu\text{m}$, respectively. Cormier et al. (2015) finds that the Pox 186 is well-centred on the brightest spaxel of their FIR maps and hence reports FIR emission line fluxes by applying a point-source correction to the brightest spaxel.

For completeness, in Table 2 we tabulate the line fluxes of Pox 186 in the MIR and FIR wavelength regime taken from Cormier et al. (2015)

3 RESULTS

3.1 Source Redshift and Distance

We determine the source redshift by measuring the observed wavelength of four strong UV emission lines O III] and C III] as shown in Table 3. We do not use the strong C IV emission line because it is double-peaked (Section 4.2). We do not use the optical emission lines because the zero-point of the wavelength calibration of GMOS-N data is not very well-constrained (Kumari 2018). The redshift of

Table 4. Equivalent widths and emission line fluxes (observed F_λ and intrinsic I_λ) of the UV nebular emission lines.

Emission lines	EW (Å)	F_λ	I_λ
C IV λ 1548	5.21 ± 0.22	0.50 ± 0.02	0.99 ± 0.09
C IV λ 1550	2.54 ± 0.18	0.27 ± 0.02	0.53 ± 0.06
He II λ 1640	–	$<0.08^a$	$<0.16^a$
O III] λ 1660	2.21 ± 0.29	0.23 ± 0.03	0.43 ± 0.06
O III] λ 1666	5.74 ± 0.38	0.58 ± 0.04	1.08 ± 0.11
C III] λ 1907, 1909	35.85 ± 0.73	2.56 ± 0.05	4.4 ± 0.3

Notes: Fluxes are in units of $\times 10^{-14} \text{ erg s}^{-1} \text{ cm}^{-2}$.

^a 2σ upper-limit

Pox 186 is 0.0040705 ± 0.000013 from the presented HST/COS data and agrees with that of Guseva et al. (2004) and Eggen et al. (2021) within uncertainties. At $H_o = 70 \text{ km s}^{-1}$ and $\Omega_m = 0.3$, the observed redshift corresponds to a luminosity distance of 17.5 Mpc, and an angular scale of 84.1 pc per arcsec. However, we derive a value of 12.6 Mpc if we use Cosmicflows-3 (Kourkchi et al. 2020).

3.2 Line fluxes and equivalent widths

3.2.1 UV

Table 4 presents the fluxes and equivalent widths (EW) of the UV emission lines O III], C III] and C IV. We estimate fluxes by summing the fluxes in the spectral line after subtracting a local linear continuum fitted to either side of the three doublets. The continuum level at the central wavelength of each emission line is used to estimate their equivalent widths. We correct the UV emission line fluxes using the E(B-V) value determined from optical Balmer decrement which is described later in Section 3.3.

3.2.2 Optical

We want to compare the UV, optical, MIR and FIR properties of Pox 186 together for which we need to take into account the varying aperture sizes or FOVs of the different instruments with which these four different datasets are acquired. The GMOS-IFU data allow us to probe the optical properties for different apertures and sizes. We chose to extract two sets of integrated spectra. The first one is obtained by integrating all GMOS spectra within a circular aperture of $1.25''$ radius centred on the brightest knot of Pox18, hence coinciding with the HST/COS aperture, and is referred to as ‘COS-matched integrated’ spectra. While the second set of spectra is obtained by integrating all spectra within the GMOS-IFU FOV and is referred to as ‘Gemini-FOV integrated’ spectra. The main difference between the two sets of spectra is that the COS-matched integrated spectra only include the compact core of Pox 186, and exclude its plume, unlike the Gemini-FOV integrated spectra which include both. Figure 4 shows the COS-matched integrated spectra along with several optical and NIR emission lines.

We measure the emission line fluxes for the recombination and collisionally excited emission lines (except $H\alpha$ and [O III] λ 5007) within the integrated spectra by fitting single Gaussian profiles after subtracting a linear continuum in the spectral region of interest via custom-written python codes using LMFIT package (Newville et al. 2014). Equal weight is given to flux in each spectral pixel while fitting Gaussians and the fitting uncertainties on the Gaussian parameters are propagated to calculate the flux uncertainty. We also create emission line flux maps for all lines (including $H\alpha$ and [O III] λ 5007) of the

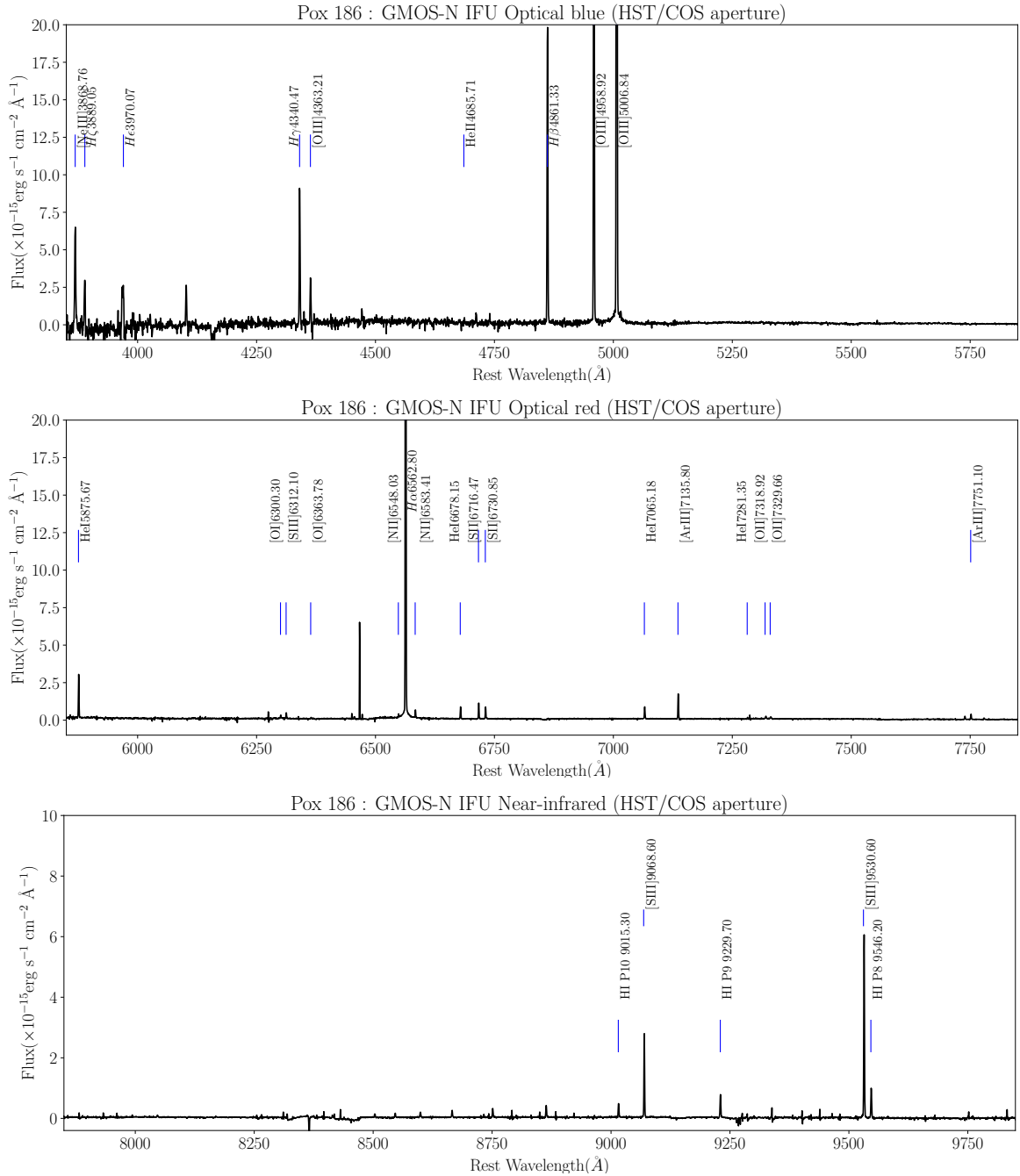


Figure 4. GMOS-N IFU integrated spectra of Pox 186 obtained by summing the spatially-resolved spectra within a circular aperture of radius $1.25''$ overlapping with the COS aperture covering a rest-frame wavelength range of $\sim 3800\text{--}9900\text{\AA}$. The important optical emission lines are marked in blue. We have also marked the location of He II 4686, which remains undetected in the optical spectrum.

entire GMOS FOVs in the same way, which are shown in Appendix C (Figures C1 and C3).

The strong emission lines $H\alpha$ and $[\text{O III}]\lambda 5007$ show a weak broad component in the integrated spectra matching COS aperture. We estimate the $H\alpha$ line flux by summing the fluxes under the line within the continuum subtracted spectrum and removing the flux contribution from the $[\text{N II}]$ lines in the wings of $H\alpha$ broad component. The wing of $[\text{O III}]\lambda 5007$ also shows the He I 5015 line, which we remove by modelling it with a Gaussian from the continuum subtracted spectrum. This spectrum is then used to estimate $[\text{O III}]\lambda 5007$ line

flux by summing over the fluxes under the line. Table 5 presents the measured observed line fluxes for the emission lines measured in the two sets of the integrated GMOS spectra, the COS-matched integrated spectra ($F_{\lambda}(\text{COS})$) and the Gemini-FOV integrates spectra ($F_{\lambda}(\text{Gemini FOV})$). The uncertainties on the emission line fluxes presented in the Table are the random measurement uncertainties. However, we also include a systematic flux uncertainty of 50% (see Appendix B) and propagate in the inferred properties whenever it becomes relevant in the analysis, and is explicitly mentioned in the paper.

Table 5. Optical emission line flux measurements (relative to $H\beta = 100$) obtained from the two sets of integrated Gemini/IFU spectra: (i) the one overlapping with the COS aperture (ii) the other from the entire Gemini FOV. Observed line fluxes (F_λ) are extinction-corrected using E(B-V) to calculate the intrinsic line fluxes (I_λ).

Line	λ_{air}	F_λ (COS)	I_λ (COS)	F_λ (Gemini FOV)	I_λ (Gemini FOV)
H γ	4340.47	45.18 ± 1.27	46.59 ± 2.28	42.54 ± 3.06	44.40 ± 2.90
[OIII]	4363.21	14.38 ± 0.77	14.81 ± 0.89	12.93 ± 1.84	13.47 ± 2.17
H β	4861.33	100.00 ± 0.59	100.00 ± 2.87	100.00 ± 1.12	100.00 ± 2.26
[OIII]	4958.92	212.80 ± 1.50	211.71 ± 7.74	216.59 ± 2.82	215.04 ± 8.85
[OIII]	5006.84	637.53 ± 3.98	632.70 ± 20.53	645.74 ± 7.81	638.95 ± 23.62
HeI	5875.67	12.29 ± 0.14	11.78 ± 0.39	12.12 ± 0.22	11.43 ± 0.30
[OI]	6300.3	1.01 ± 0.09	0.96 ± 0.08	1.09 ± 0.23	1.01 ± 0.19
[SIII]	6312.1	1.46 ± 0.11	1.38 ± 0.12	1.49 ± 0.27	1.38 ± 0.26
[NII]	6548.03	0.71 ± 0.15	0.67 ± 0.11	0.80 ± 0.16	0.74 ± 0.13
H α	6562.8	303.97 ± 1.84	286.00 ± 9.24	311.30 ± 3.74	286.00 ± 8.27
[NII]	6583.41	2.14 ± 0.44	2.01 ± 0.34	2.41 ± 0.47	2.21 ± 0.40
HeI	6678.152	2.78 ± 0.06	2.61 ± 0.10	2.67 ± 0.13	2.44 ± 0.11
[SII]	6716.47	3.67 ± 0.07	3.44 ± 0.11	3.99 ± 0.16	3.64 ± 0.17
[SII]	6730.85	2.81 ± 0.07	2.64 ± 0.09	3.15 ± 0.16	2.88 ± 0.19
[ArIII]	7135.8	6.81 ± 0.09	6.32 ± 0.20	7.20 ± 0.20	6.49 ± 0.22
[OII]	7318.92	0.97 ± 0.08	0.89 ± 0.07	18.47 ± 0.54	16.55 ± 0.63
[OII]	7329.66	0.85 ± 0.07	0.79 ± 0.05
HI P10	9017.4	2.09 ± 0.06	1.88 ± 0.06	-	-
[SIII]	9068.6	11.45 ± 0.11	10.25 ± 0.12	-	-
[SIII]	9530.6	26.64 ± 0.23	23.7 ± 0.2	-	-
E(B-V)		0.059 ± 0.007		0.083 ± 0.009	
F(H β)		40.76 ± 0.23		48.12 ± 0.54	

Notes: F(H β) in units of $\times 10^{-15}$ erg cm $^{-2}$ s $^{-1}$.
 ...: S/N < 3 for a given line.

-: For these lines, the covered Gemini FOV is different than for the rest of the emission lines, hence we do not report their values.

Table 6. Summary of physical properties obtained from the Gemini optical integrated spectra and the COS UV spectra (value±uncertainty)

Parameter	Value
[O III]/H β	0.805 ± 0.003
[N II]/H α	-2.15 ± 0.09
[S II]/H α	-1.671 ± 0.007
EW([O III] $\lambda\lambda$ 4959,5007+H β) (Å)	1800 ± 800
EW(H α) (Å)	820 ± 20
β -slope	-0.36 ± 0.02
T_e ([OIII]) ($\times 10^4$ K)	1.63 ± 0.05
T_e ([OII]) ($\times 10^4$ K)	1.39 ± 0.08
N_e ([SII]) (cm $^{-3}$)	110 ± 30
12 + log(O $^+$ /H $^+$)	7.22 ± 0.12
12 + log(O $^{2+}$ /H $^+$)	7.76 ± 0.04
12 + log(O/H)	7.87 ± 0.04
C $^{2+}$ /O $^{2+}$	0.21 ± 0.03
C $^{3+}$ /O $^{2+}$	0.041 ± 0.004
log(C/O) direct	-0.59 ± 0.04
log(C/O) empirical	-0.60 ± 0.03
T_{eff}^\ddagger (kK)	60 ± 18
log \mathcal{U}^\ddagger	-2.4 ± 0.4
log (q/cm s $^{-1}$) ‡	8.1 ± 0.4
log \mathcal{U}^\star	-2.661 ± 0.014

Notes: \ddagger : Output from HCM-TEFF assuming spherical geometry. \star : Ionization parameter using [S III]/[S II] calibration from Kewley et al. (2019).

3.3 Reddening correction

We estimate the colour excess E(B-V), by using the attenuation curve of the Small Magellanic Cloud (SMC; Gordon et al. 2003) along with the observed Balmer decrement (H α / H β) assuming a Case B recombination and an electron temperature and density of 10 4 K and 100 cm $^{-3}$, respectively. We estimate E(B-V) for both sets of integrated optical spectra, the one overlapping with COS and the other one corresponding to the entire GMOS FOV. The E(B-V) for the COS-matched integrated spectra is 0.053 ± 0.004 which is close to the E(B-V) of the Milky Way in the line-of-sight of Pox 186, i.e., 0.0385 ± 0.0016 (Schlafly & Finkbeiner 2011), hence indicating a very low amount of dust in the central region of Pox 186.

The intrinsic fluxes for the UV and optical lines are estimated by correcting the observed line fluxes using the E(B-V). No reddening correction is done for the MIR or FIR emission line fluxes. Table 4 presents the intrinsic fluxes of the emission lines of the UV COS spectra, while Table 5 shows the intrinsic fluxes for the COS-matched and Gemini-FOV integrated spectra. The uncertainties on the intrinsic fluxes are derived from propagating the random uncertainties on fluxes measured while fitting the emission lines.

3.4 Physical properties of ionized gas and ionizing stellar population

3.4.1 Electron temperature and Density

The UV, optical and IR spectra have emission lines sensitive to the electron temperature (T_e) and density (N_e). For example, the UV line O III $\lambda\lambda$ 1660,1666 is temperature-sensitive and when combined with the optical [O III] λ 5007 line, probes T_e . Similarly, the optical line ratio of [O III] λ 4363 and [O III] $\lambda\lambda$ 4959, 5007 is also sensitive to

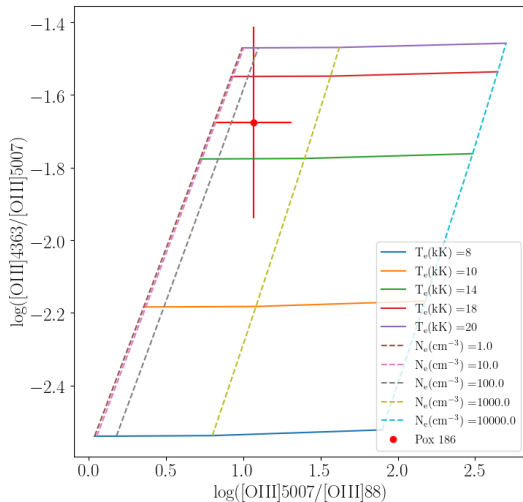


Figure 5. PYNEB grids of $[\text{O III}]\lambda 4363/[\text{O III}]\lambda 5007$ versus $[\text{O III}]\lambda 5007/[\text{O III}]\lambda 88 \mu\text{m}$ for $T_e=8\text{--}20\text{kK}$ and $N_e=1\text{--}10000 \text{ cm}^{-3}$. The red point denotes the emission line flux ratios of Pox 186, where the optical $[\text{O III}]$ emission line fluxes correspond to the entire Gemini-FOV, and the FIR $[\text{O III}]$ line is taken from Cormier et al. (2015), hence both optical and FIR datasets shown here cover the entire galaxy. The uncertainties on the line ratio include the systematic uncertainties on the optical line fluxes (see Section B).

T_e . Similarly, the optical to IR line ratio, $[\text{O III}]\lambda 5007/[\text{O III}]\lambda 88 \mu\text{m}$ is sensitive to T_e , but also to N_e (Dinerstein et al. 1985).

Figure 5 shows the optical $[\text{O III}]$ lines flux ratio ($[\text{O III}]\lambda 4363 / [\text{O III}]\lambda 5007$) versus the optical-IR $[\text{O III}]$ lines flux ratio $[\text{O III}]\lambda 5007/[\text{O III}]\lambda 88 \mu\text{m}$, where the grids are generated using the emissivities of the respective $[\text{O III}]$ lines from the PYNEB code for a set of T_e and N_e values. The grid lines are not orthogonal as $[\text{O III}]\lambda 5007/[\text{O III}]\lambda 88 \mu\text{m}$ is sensitive to both T_e and N_e . We also show the optical $[\text{O III}]$ lines flux ratio and optical-IR $[\text{O III}]$ lines flux ratio $[\text{O III}]$ of Pox 186, obtained from Gemini-FOV integrated spectra. We deem the use of Gemini-FOV integrated spectra for this comparison instead of the COS-matched integrated spectra because of the large FOV and PSF of the Herschel data (see Section 2.3) which includes not only the compact core of Pox 186 but also its plume. Note that the COS-matched integrated spectra miss the plume of Pox 186. The observed lines ratio lies on the PYNEB grids and is in contradiction to that found by Chen et al. (2023). The optical $[\text{O III}]$ emission line flux ratio for the Gemini-FOV integrated spectra corresponds to $T_e = 15000 \pm 1300\text{K}$.

From the COS-matched optical spectra, we estimate $T_e([\text{O III}]) = 16300 \pm 500\text{K}$ by using the emission line flux ratio of the auroral line $[\text{O III}]\lambda 4363$ and $[\text{O III}]\lambda 4959, 5007$. Since UV line $[\text{O III}]\lambda 1660, 1666$ is also temperature-sensitive, we also estimate $T_e([\text{O III}])$ by using the emission line flux ratio of $[\text{O III}]\lambda 5007/[\text{O III}]\lambda 1660, 1666$, which is in agreement with that obtained from optical emission line ratios. The electron temperatures derived from the COS-matched and Gemini-FOV integrated spectra agree with each other and are typical of the H II regions within the star-forming galaxies (Kumari et al. 2017, 2018, 2019).

We measure electron density using the density-sensitive line ratio $[\text{S II}]\lambda 6717, 6731$ line ratio and $T_e([\text{O III}])$ determined above for the COS-matched as well as the Gemini-FOV integrated spectra. For

both datasets, the electron density indicates a low-density regime. We note that the density-sensitive line doublets $[\text{O II}]\lambda\lambda 3727, 3729$ could not be used for determining density, as the sensitivity of GMOS-IFU in the blue end has degraded over time, and hence the blue-end data are unusable. We do not estimate N_e from the density-sensitive UV doublet $\text{C III}\lambda\lambda 1907, 1909$ available from the COS spectra as the doublet is blended and asymmetric.

3.4.2 Chemical abundances

The chemical abundances of Pox 186 are only determined for the COS-overlapping central region, because of the non-detection of the necessary emission lines in the Gemini-FOV integrated spectra.

Gas-phase metallicity: The gas-phase metallicity ($12 + \log(\text{O}/\text{H})$) can be robustly estimated from the T_e -base direct method, where the abundances of the dominant ionic states of oxygen (O^+ and O^{2+}) are first determined from the temperatures of their respective ionization zones and then combined to estimate the total oxygen abundance. The temperature of the high-ionization zone $T_e([\text{O III}])$ is determined as derived in Section 3.4.1 and is combined with $N_e([\text{S II}])$ to estimate the temperature of the low-ionization zone by using the density-dependent calibration given in Pérez-Montero (2017). Like Kumari et al. (2019) where $[\text{O II}]\lambda\lambda 3727, 3729$ remain undetected, we measure O^+/H^+ using $[\text{O II}]\lambda\lambda 7320, 7330$ and the low-ionization temperature $T_e([\text{O II}])$ by employing the formula given in Kniazev et al. (2003). We measure O^{2+}/H^+ using $[\text{O III}]\lambda\lambda 4959, 5007$ and $T_e([\text{O III}])$ in the formula given in Pérez-Montero (2017). The oxygen ionic abundances are combined to calculate the oxygen elemental abundance, $12 + \log(\text{O}/\text{H}) = 7.87 \pm 0.04$, for the region of Pox 186 probed by COS, and agrees within 3σ with that derived by Guseva et al. (2004) for a larger region of this galaxy.

Carbon-to-oxygen ratio: We follow the relations between $T_e([\text{O III}])$ and dereddened line ratios $\text{C III}/\text{O III}$ and $\text{C IV}/\text{O III}$ provided in Pérez-Montero (2017), we estimate $\text{C}^{2+}/\text{O}^{2+}$ and $\text{C}^{3+}/\text{O}^{2+}$. We estimate direct method C/O by combining $\text{C}^{2+}/\text{O}^{2+}$ and $\text{C}^{3+}/\text{O}^{2+}$, assuming $\frac{\text{C}}{\text{O}} = \frac{\text{C}^{2+} + \text{C}^{3+}}{\text{O}^{2+}}$. We also estimate C/O using the empirical method given in (Pérez-Montero 2017). The estimates of C/O from the direct and empirical method are in excellent agreement with each other (Table 6).

3.4.3 Ionization parameter and Effective Temperature

For estimating the ionization parameter ($\log \mathcal{U}$) and effective temperature (T_{eff}) of the central region matching COS-aperture, we use the publicly available code HCM-TEFF CODE (v5.3 Pérez-Montero et al. 2019) where we assume a blackbody model and use reddening-corrected optical emission line fluxes ($[\text{O III}]\lambda\lambda 4959, 5007, [\text{S II}]\lambda\lambda 6717, 6731, \text{He I}\lambda 6678, \text{Ar I}\lambda 7135, [\text{S III}]\lambda\lambda 9069, 9532$) from the COS-matched integrated and the gas-phase metallicity ($12 + \log(\text{O}/\text{H}) = 7.87 \pm 0.04$, Section 3.4.2), and run the code for plane-parallel and spherical geometry separately. We find that the choice of geometry has no effect on either $\log \mathcal{U}$ or T_{eff} for the central region of Pox 186. We also estimate $\log \mathcal{U} = -2.661 \pm 0.014$ using the calibration involving $[\text{S III}]\lambda\lambda 9069, 9532/[\text{S II}]\lambda\lambda 6717, 6731$ given by Kewley et al. (2019), which agrees with that derived from HCM-TEFF.

For determining $\log \mathcal{U}$ for the entire Pox 186 galaxy, we use calibrations from Kewley et al. (2019) including the MIR line ratios (Table 2), $[\text{Ne III}]/[\text{Ne II}]$ which gives $\log \mathcal{U} = -2.55 \pm 0.22$. Note that we do not use optical line ratio $[\text{S III}]/[\text{S II}]$ mainly because $[\text{S III}]\lambda\lambda 9069, 9530$ lines cover a slightly different FOV than the rest

of the optical emission lines including [S II]. It is for the same reason that we could not use HCM-TEFF to estimate these two parameters for the Gemini FOV.

3.4.4 Radiation hardness

Hardness of the radiation field can be measured by the softness parameter $\log \eta$. It was initially defined in terms of optical ionic ratios $\eta = (O^+/O^{2+})/(S^+/S^{2+})$ (Vilchez & Pagel 1988), and can be estimated from the calibration provided in Kumari et al. (2021), i.e., $\log \eta = \log \eta' + 0.16/t + 0.22$, where $t = T_e/10^4$ and $\log \eta'$ can be determined from the optical emission line ratios ($\log \eta' = \frac{[O II]}{[S II]} / \frac{[O III]}{[S III]}$) or the MIR infrared line ratios ($\log \eta' = \frac{[Ne II]}{[S III]} / \frac{[Ne III]}{[S IV]}$) as mentioned in Pérez-Montero & Vilchez (2009).

We estimate $\log \eta' = -0.47 \pm 0.23$ using MIR emission line fluxes (Table 2). We estimate $\log \eta = -0.14 \pm 0.23$ using T_e from the Gemini-FOV integrated spectra and $\log \eta'$ estimated earlier. We chose to use T_e from the Gemini-FOV integrated spectra rather than COS-matched integrated spectra as the former covers the entire galaxy like MIR data. We do not use the optical emission line fluxes to determine $\log \eta'$ as [O II] $\lambda\lambda$ 3729, 3729 are not detected because of the decreased sensitivity of GMOS-N IFU in the blue wavelength end. Lower $\log \eta$ and $\log \eta'$ indicate a hard radiation field. Pox 186 exhibits lower values of $\log \eta'$ and $\log \eta$ compared to the average values exhibited by star-forming regions or galaxies in the local Universe (Kumari et al. 2021), thus indicating that the radiation field in Pox 186 is harder than average.

Table 6 summarizes all the physical properties derived in this section. The uncertainties on the derived quantities are estimated from the random uncertainties on the flux measured while fitting emission lines and excluding the systematic flux uncertainty.

4 DISCUSSION

4.1 Large equivalent widths of nebular carbon lines

We find $EW(C III)\lambda\lambda$ 1906,1909 = $35.85 \pm 0.73 \text{ \AA}$ for Pox 186. Figure 6 shows a comparison of $EW(C III)\lambda\lambda$ 1906,1909 versus $EW([O III]\lambda\lambda$ 4959,5007+ $H\beta$) for Pox 186 with galaxies at $z \sim 0-4$. We find that Pox 186 exhibits the highest $EW(C III)$ among all the star-forming galaxies in the local Universe ($z \sim 0$, Leitherer et al. 2011; Senchyna et al. 2017, 2019, Figure 6), and the majority of the star-forming galaxies at the intermediate ($z \sim 2-4$, Erb et al. 2010; Stark et al. 2014; Vanzella et al. 2016; Maseda et al. 2017; Vanzella et al. 2017; Tang et al. 2021). However, $EW(C III)$ is also reported to lie within 20–40 \AA for a small fraction ($\sim 1.2\%$) of star-forming galaxies at the intermediate ($z \sim 2-4$, Le Fèvre et al. 2019) and a few EoR galaxies ($z \geq 6$, Stark et al. 2017; Hutchison et al. 2019; Topping et al. 2021; Jiang et al. 2021).

We also measure the $EW(C IV)\lambda\lambda$ 1548,1550 = $7.75 \pm 0.28 \text{ \AA}$ for Pox 186, which is comparable to those found for local metal-poor galaxies with very young stellar populations (Berg et al. 2016, 2019; Senchyna et al. 2019).

We explore the cause for the extreme EW of carbon lines in the following:

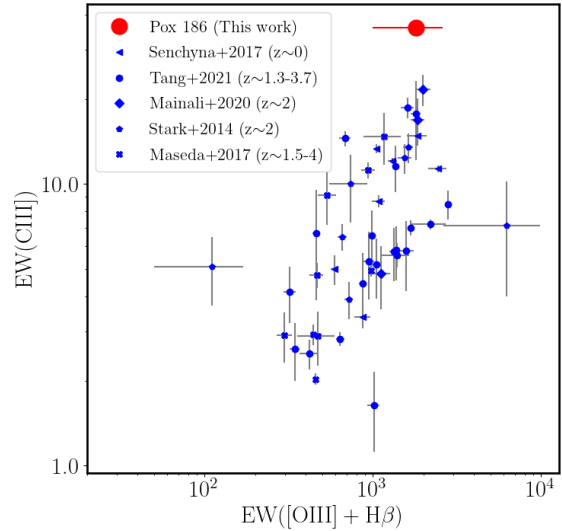


Figure 6. $EW(C III)$ versus $EW([O III] + H\beta)$ for Pox 186 (red dot) compared with galaxies at $z \sim 0-4$, taken from Stark et al. (2014); Maseda et al. (2017); Senchyna et al. (2017); Mainali et al. (2020); Tang et al. (2021)

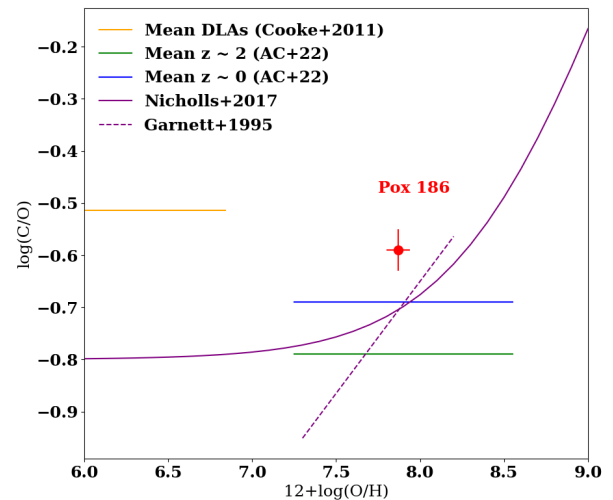


Figure 7. C/O versus O/H for Pox 186, along with average C/O for $z \sim 0$ (horizontal blue line) and $z \sim 2$ (horizontal green line) from Arellano-Córdova et al. (2022) and for DLAs from Cooke et al. (2011). The solid and dashed purple lines indicate the C/O-O/H relation given in Nicholls et al. (2017) and Garnett et al. (1995), respectively.

4.1.1 High effective temperature

Nakajima et al. (2018) states that $EW(C III)] > 30 \text{ \AA}$ can be caused by blackbody with extremely high effective temperature (T_{eff}), i.e. $> 6 \times 10^4 \text{ K}$. We estimate $T_{\text{eff}} = 60 \pm 18 \text{ kK}$ assuming blackbody using the HCM-TEFF code (Section 3.4.3), thus indicating that the high effective temperature may be responsible for high carbon EW observed for Pox 186.

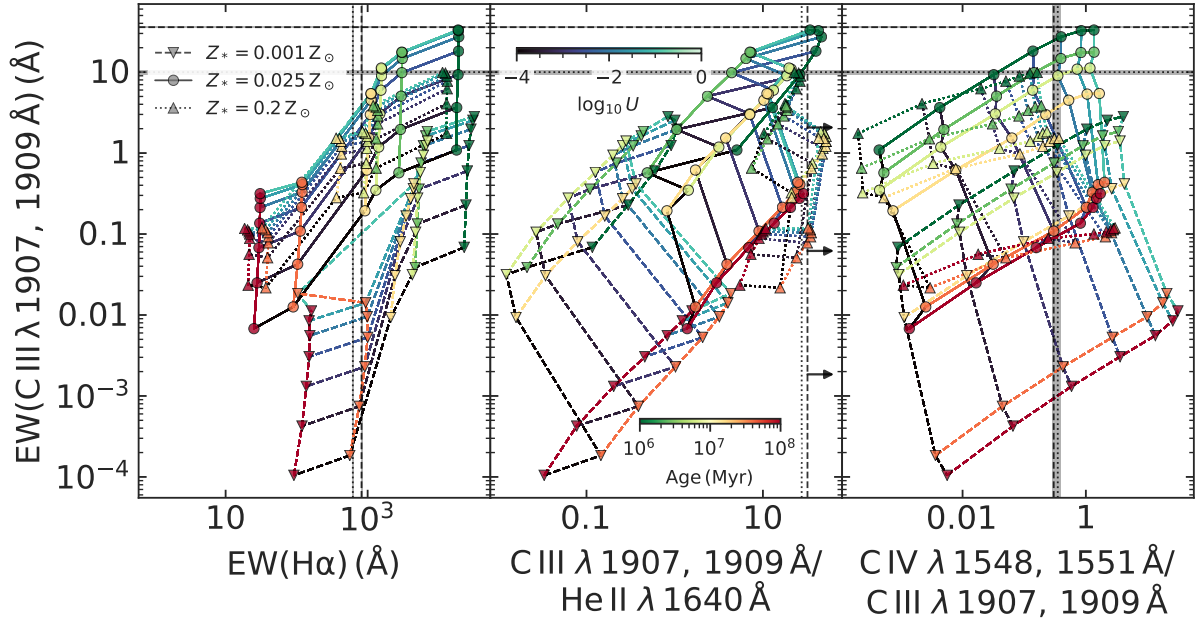


Figure 8. EW(C III) plotted against EW(H α) (left-hand panel), C III/He II 1640 line ratio (middle panel) and C IV/C III (right-hand panel) using the CLOUDY models described in Section 4.1.3. The horizontal dashed line indicates the observed EW(C III) while the horizontal dotted line indicates the reddening-corrected EW(C III) where line flux is corrected using nebular E(B-V) while continuum is corrected using the stellar E(B-V). Similarly, the vertical dashed and dotted lines indicate the observed and reddening-corrected quantities, respectively. The reddening-corrected EW is obtained by using nebular E(B-V) for line fluxes and stellar E(B-V) for continuum, while the reddening-corrected emission line ratios are obtained by using nebular E(B-V) for both emission lines in the ratio. The right-ward pointing arrows in the middle panel indicates the lower limit on the C III/He II where a 2σ -upper limit on He II line is considered.

4.1.2 High carbon-to-oxygen ratio

Jiang et al. (2021) suggests that the high EW(C III) and EW(C IV) could be due to a higher carbon abundance.

We explore this via Figure 7, which shows that the C/O abundance of Pox 186 (red point) is higher than the average for galaxies found in the same metallicity range at $z \sim 0$ (horizontal blue line) and $z \sim 2$ (horizontal green line) from Arellano-Córdova et al. (2022). It is also higher than that predicted by the best-fit line to C/O versus O/H for measurements of stars derived by Nicholls et al. (2017, solid purple curve) and for measurements of irregular dwarf galaxies derived from Garnett et al. (1995, dashed solid line). Thus, the higher C/O for Pox 186 supports the argument from Jiang et al. (2021) about higher carbon abundance causing the higher EW of carbon lines.

We note that the optical spectrum of Pox186 does not show any signature of the carbon-rich Wolf-Rayet (WR) stars either as red or blue WR bump which could lead to a direct enhancement of carbon. Schaerer et al. (1999) lists Pox 186 as a WR galaxy on the basis of a broad He II λ 4686 at 0.8σ above background reported in Kunth & Joubert (1985). The high-quality HST/COS and GMOS-IFU data allow us to exclude Pox 186 as a WR candidate.

4.1.3 Slope and upper mass of top-heavy initial mass function

To understand the origin of the extreme EW(C III) measured in Pox186, we consider CLOUDY models broadly similar to those in Witstok et al. (2022); here, we give a brief summary and highlight the differences with the models presented in Witstok et al. (2022). The incident radiation field of a single burst of star formation with varying ages (1 Myr to 100 Myr) is generated by BPASS v2.1 stellar population synthesis models including binary stars under a top-heavy initial mass function (IMF; with slope -2 ; Eldridge et al. 2017),

ranging in stellar mass from $1 M_\odot$ to $300 M_\odot$. Unlike in Witstok et al. (2022), calculations stop when a molecular fraction of 10^{-6} is reached, such that the model does not extend into a photodissociation region beyond the central H II region.

We considered models with a wide range of base (stellar) metallicities, tuning the gas-phase metallicity to match the observed values of Pox186. We introduce an additional nebular α /Fe enhancement, which is accomplished by increasing the nebular abundances of individual α elements (for details, we refer to Witstok et al. 2022). The nebular elemental abundances of the main α elements (C, O, Ne, Mg, Si, S) are scaled up by $4\times$, except for carbon which is increased by a factor of 2, so that the C/O ratio is approximately half the solar value as appropriate for Pox186 (see Section 4.1.2). Moreover, this implies our fiducial model with stellar metallicity $Z_* = 0.025 Z_\odot$ has a nebular oxygen abundance of approximately 10% solar, as directly measured for Pox186 (see Section 4.1.2). We vary the ionisation parameter and hydrogen density between $-4 < \log_{10} U < -1$ and $10^{-1} \text{ cm}^{-3} < n_H < 10^4 \text{ cm}^{-3}$ (as measured at the illuminated face of the cloud), respectively.

An overview of the models generated in CLOUDY is shown in Figure 8. For simplicity, we only show models with a fixed density of $n_H = 10^2 \text{ cm}^{-3}$ and stellar metallicities of $0.001 Z_\odot$, $0.025 Z_\odot$, and $0.2 Z_\odot$. We find particularly the slope and upper mass of the IMF are restrictive in reproducing the extreme EWs of C III], as models with an upper mass of $100 M_\odot$ only reach EWs of approximately 20 \AA^3 . However, none of these models could simultaneously reproduce the

³ For comparison, in Appendix D, we present the models using an upper mass of $300 M_\odot$ and slope -2.3 and no α /Fe enhancement which reproduce EW(C IV) and not the EW(C III)].

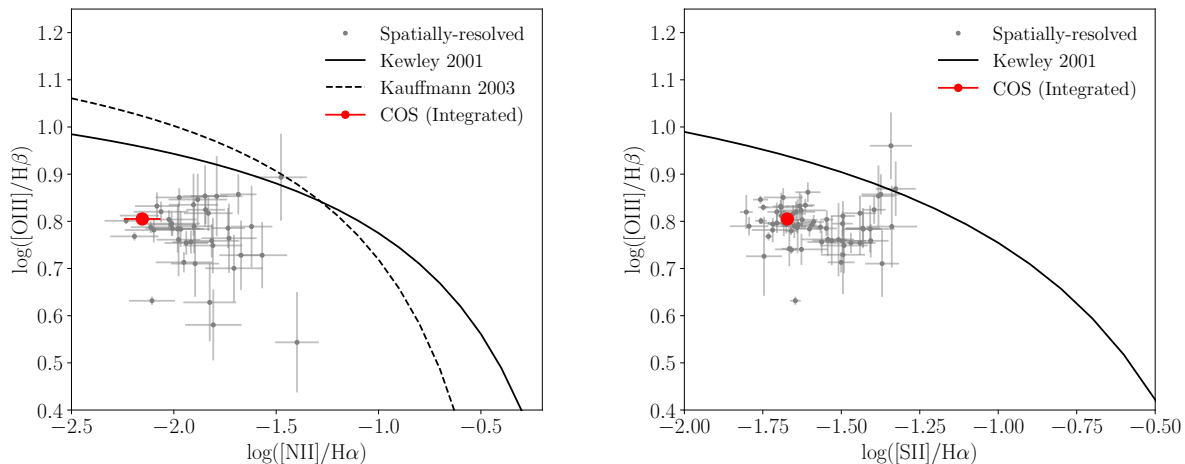


Figure 9. Classical optical emission line ratio diagrams: $[\text{O III}]/\text{H}\beta$ versus $[\text{N II}]/\text{H}\alpha$ (left-hand panel) and $[\text{O III}]/\text{H}\beta$ versus $[\text{S II}]/\text{H}\alpha$ (right-hand panel). Black solid curve and dashed curve represent the maximum starburst line from Kewley et al. (2001, theoretical) and Kauffmann et al. (2003, empirical), respectively, distinguishing between the photoionized and non-photoionized regions. The blue dot denotes the corresponding emission line ratios obtained from the optical spectra integrated over the COS aperture, while the grey dots indicate the spatially-resolved emission line ratios.

observed EW of $\text{C III}]$ and $\text{H}\alpha$ emission lines, denoted by dashed horizontal and vertical lines, respectively, in Figure 8).

To explore this further, we considered the dust distribution which might affect the nebular $\text{C III}]$ and the underlying stellar continuum differently. We estimate the UV continuum slope $\beta = -0.36 \pm 0.02$ using the spectral windows from Calzetti et al. (1994) in the wavelength region of $\sim 1250\text{--}1850$, which indicates a red continuum. If we use this β value to deredden the continuum using the SMC law from Reddy et al. (2018) and use $E(B-V)$ derived from the optical data to deredden the emission line again using the SMC law, the $\text{EW}(\text{C III}]$ may decrease by a factor of 3. The reddening-corrected values are shown by dotted vertical and horizontal lines, which can not be reproduced by the models either.

The inability of the models to reproduce the observed or reddening-corrected properties of Pox 186 could be due to the simplistic assumptions on the geometry and relative distribution of dust and gas within the photoionization models. In summary, it indicates the need to improve the existing population synthesis and photoionization models.

4.1.4 Hard Ionizing Radiation

High $\text{EW}(\text{C III}]$ is also proposed to be caused by the hard ionizing radiation from extreme stellar populations or AGN (Nakajima et al. 2018; Jiang et al. 2021) or shocks from the radio jets (Best et al. 2000). We rule out the possibility of an AGN/shocks causing the high $\text{EW}(\text{C III}]$ as figure 9 shows that the optical emission line ratios obtained from the integrated spectrum, $[\text{O III}]/\text{H}\beta$ versus $[\text{N II}]/\text{H}\alpha$ (left-hand panel) and $[\text{O III}]/\text{H}\beta$ versus $[\text{S II}]/\text{H}\alpha$ (right-hand panel) do not occupy the AGN/shock region of the classical emission-line diagnostic diagrams (Baldwin et al. 1981; Veilleux & Osterbrock 1987). Figure 9 also shows a few spaxel-based line ratios lying beyond the photoionization region on the BPT diagrams; however, they are too few ($\sim 2.5\%$ and $\sim 3\%$ for $[\text{N II}]$ -BPT and $[\text{S II}]$ -BPT diagrams, respectively) to be a conclusive indicator of hard AGN radiation. Hard ionizing radiation is also expected to produce He II lines, so emission line ratio diagnostic diagrams including optical and UV He II lines are also used to determine the presence of AGN (Feltre et al. 2016; Brinchmann et al. 2008). However, nei-

ther $\text{He II } \lambda 1640$ nor $\text{He II } \lambda 4686$ lines are detected in the spectrum corresponding to the COS pointing. The above discussion shows that hard ionizing radiation from AGN is unlikely to be the cause of high $\text{EW}(\text{C III}]$.

4.2 Line profiles of carbon lines

Figure 10 (left-hand panel) shows that C IV line profile is broadened with respect to $\text{O III}]$ line profile, which appears to be caused by collisional excitation. Berg et al. (2019) observed similar behaviour in a couple of local metal-poor galaxies and attributed this to the resonant scattering nature of C IV . However, for Pox 186, we find that $\text{C III}]$ line is also broadened with respect to $\text{O III}]$ (Figure 10, right-hand panel). Given that the $\text{C III}]$ is not reported to come from resonant scattering, we rule out resonant scattering as the cause of broadening in carbon lines.

It is unlikely that outflows could cause broadening in carbon emission lines because outflows would lead to broadening in all emission lines in the same way, which would result in similar line profiles (i.e., including $\text{O III}]$). Still, we explore the outflows signatures in Figure 11, where we overplot the $[\text{O III}]$ emission line (normalized by its peak flux) along with $\text{Si II } \lambda 1260$ (normalized by the median flux within the local spectral region). Both $[\text{O III}]$ and $\text{Si II } \lambda 1260$ lines are centered at $\sim 0 \text{ km s}^{-1}$, showing no signatures of outflow. However, a hint of ionized gas suffering turbulence is present in the line profile of $\text{H}\alpha$ shown in Figure 12, which shows the presence of a broad underlying component of $\text{H}\alpha$ along with a narrow component.

Figure 13 shows the velocity profile of the resonantly scattered $\text{C IV } \lambda\lambda 1548, 1550$ doublet. The distinct blue and red peaks exhibited by both C IV emission lines are quite interesting, as no previous studies have ever resolved the two peaks in both emission lines of the C IV doublet, though the stronger $\text{C IV } \lambda 1548$ has been reported to have double peaks (Berg et al. 2019). The origin of double-peaked C IV is difficult to understand because C IV line profile will be impacted by the relative fraction of the gas emitting the narrow nebular emission and the foreground ISM resulting in absorption. We address two possible scenarios here: (1) a pure nebular emission

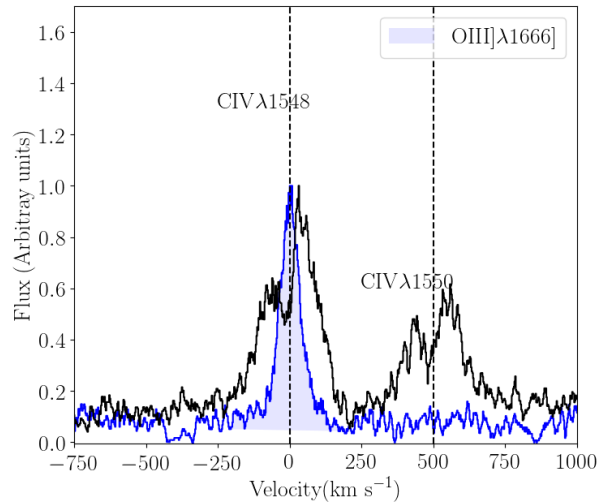
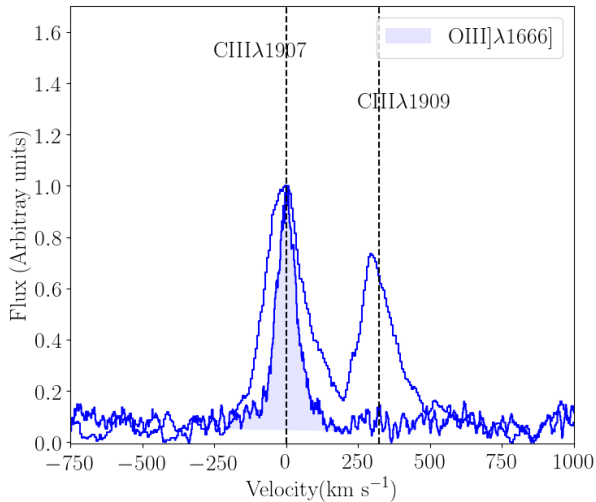


Figure 10. Comparison of O III]λ 1666 line with respect to C III]λ 1907 (left-hand panel) and C IV]λ 1548 (right-hand panel). In both panels, all emission lines (C IV]λ 1548, O III]λ 1666 and C III]λ 1907) are normalized by their peak fluxes.

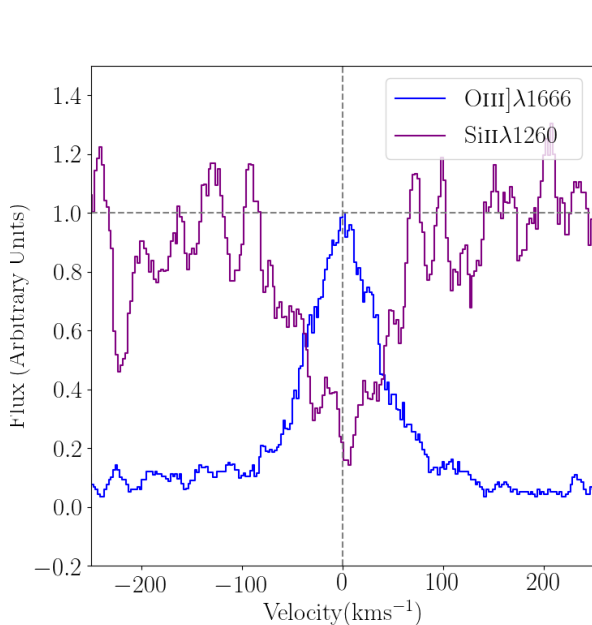


Figure 11. Comparison of velocity profiles of O III]λ 1666 emission line (blue curve) and Si II]λ 1260 absorption line (purple curve), where O III]λ 1666 is normalized by its peak flux, and Si II]λ 1260 is normalized by the median flux in the velocity range of -250 to 250 km s $^{-1}$. No signature of outflow is present.

with no ISM absorption and (2) nebular emission along with ISM absorption.

For modelling a purely nebular C IV] (Figure 13, left panel), we fit two Gaussian components to each C IV] emission line consisting of a blue-shifted (dashed-blue fit) and a redshifted component (dashed-red fit). The peak separation between the blue and the red peak (V_{sep}) is $\sim 132 \pm 2$ km s $^{-1}$ for each C IV] line, which is ~ 25 km s $^{-1}$ (on average) higher than those found by Berg et al. (2019) for two local

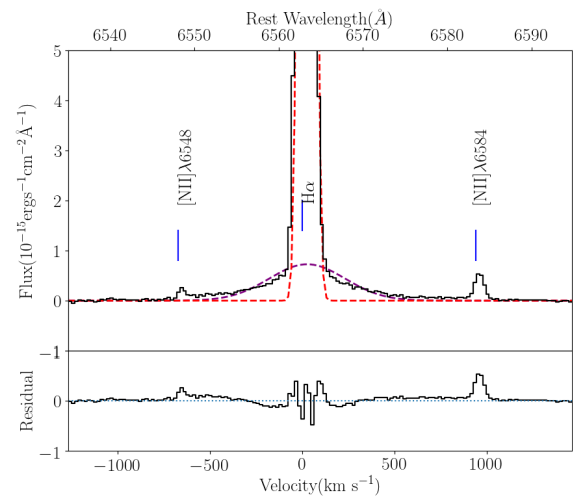


Figure 12. A narrow (purple Gaussian) and a broad (red Gaussian) component is needed to reproduce the H α line profile, hinting towards the ISM turbulence within Pox 186.

dwarf irregular galaxies. We note that the redshifted component is broader than the blue-shifted component.

For modelling the second scenario comprising of nebular emission and interstellar absorption (Figure 13, right panel), we model the emission in each C IV] line with a Gaussian profile (dashed-blue fit) and interstellar absorption via the Voigt profile (dashed-red fit). The Voigt profile corresponding to the ISM absorption is narrower compared to the broad Gaussian profile, pointing towards a lower fraction of foreground high ionization gas along the line of sight.

4.3 Stellar Winds

Stellar winds originate from hot and massive stars, i.e., with masses $> \sim 40 M_{\odot}$ and temperatures $> 25,000$ K, and lead to P Cygni-type

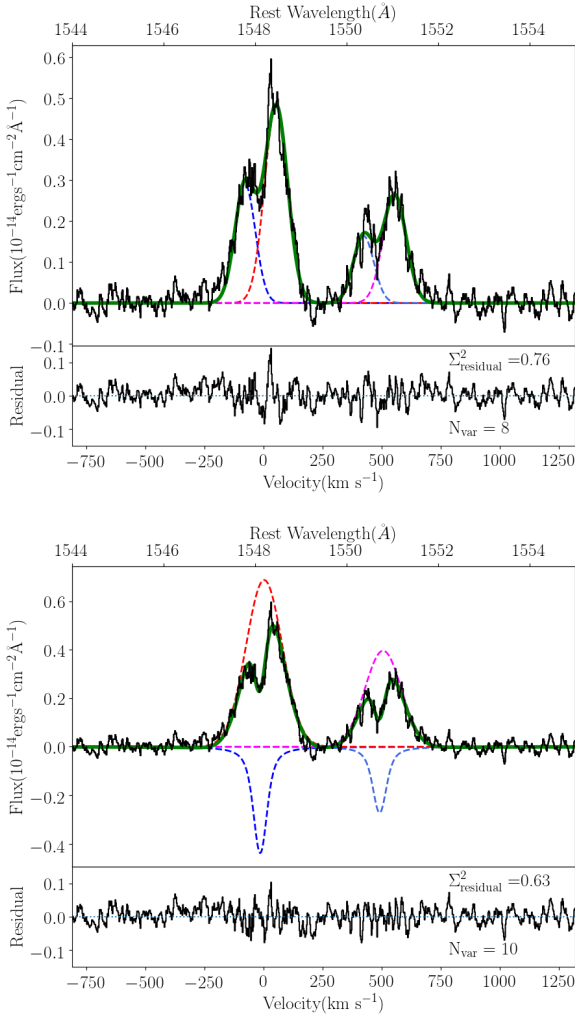


Figure 13. We model the resonantly scattered double-peaked C IV λ 1548, 1550 doublet according to two possible scenarios: (1) Purely emission without any absorbing foreground interstellar medium in the line of sight (left-hand panel), for which we model the C IV doublet via multi-component Gaussian fits to identify the peaks of the blue-shifted (dashed blue curve) and the red-shifted (dashed red) components. (2) Nebular emission along with interstellar absorption (right-hand panel), where we model the C IV nebular emission via single Gaussian (dashed red curve) and the interstellar absorption via Voigt profile (dashed blue curve). On both panels, the overall best fit is given by the solid green line.

UV line profiles, typically for the strongest lines, N v λ 1240, Si iv λ 1400 and C iv λ 1550. The UV spectra of Pox 186 show a strong P-Cygni N v λ 1400 feature (Figure 3a, 1st row), no Si iv λ 1400 and a weak P-Cygni C iv λ 1550 feature (Figure 3a, 3rd row). The weaker C iv λ 1550 compared to N v λ 1240 at lower metallicities, is indicative of a lower wind density and velocity (Leitherer et al. 2001, 2010). It is likely that the early O main-sequence stars are the main constituent of Pox 186, since these stars do not display wind effects in Si iv λ 1400, but in N v λ 1240 and C iv λ 1550 as we find in Pox 186 spectra.

Figure 14 shows the BPASS models (v2.1, IMF slope = -2.35 and upper stellar mass-limit = 300 M_{\odot}) overlaid on C IV P-Cygni profile (normalized by the continuum at $\lambda \sim 1560\text{--}1570\text{\AA}$) both for the single stars (left-hand panel) and binary stars (right-hand panel) pop-

ulation for stellar ages varying from 1–2.5 Myr and metallicity of $Z = 0.05Z_{\odot}$. It appears that the stellar populations as young as 1.6 Myr are sufficient to reproduce the weak C IV P-Cygni profile. The inclusion of binary stars has no effect on the overall C IV profile, as the binary stellar population becomes more important only at later ages (3–5 Myr) (Eldridge et al. 2020).

The blue-ward absorption in the N v P-Cygni is blended with the Ly α absorption from Pox 186 which is itself blended with the Ly α absorption from the MW. Before comparing the N v P-Cygni with the stellar population syntheses models such as BPASS, it is necessary to model and remove the Ly α absorption from Pox 186 and the MW, which requires careful modelling of the stellar continuum. We will present the detailed modelling of these components in a follow-up paper.

4.4 Implications for JWST+ALMA studies of early galaxies

4.4.1 Apparent absence of Ly α

The absence of resonantly-scattered Ly α emission in spite of strong C III] and C IV emissions is worth-noting (Figure 3a, upper-panel). A positive correlation is suggested/expected between EW(C III]) and EW(Ly α) by a few studies (e.g., Stark et al. 2014), though Rigby et al. (2015) suggest that a positive correlation exists for strong emitters with $\text{EW}(\text{C III])} > 5\text{\AA}$ and $\text{EW}(\text{Ly}\alpha) > 50\text{\AA}$, with correlation getting weaker for weaker emitters. Given that Pox 186 shows the highest EW(C III]) detected in the local Universe so far, we expect at least some Ly α emission. Similarly, Berg et al. (2019) propose that the double-peaked structure of resonantly-scattered C IV emission could be associated with a double peak in Ly α as well. Moreover, Pox 186 shows $\log \mathcal{U} = -2.4 \pm 0.4$ by or $\log(q/\text{cm s}^{-1}) = 8.1 \pm 0.4$, which lies in the range of $z \sim 2\text{--}3$ Ly α emitters (Nakajima & Ouchi 2014) further suggesting that Pox 186 could be a Ly α emitter. To investigate this further, we inspected the UV spectrum of Pox 186 taken with Space Telescope Imaging Spectrograph (STIS/HST) dataset (PI: Corbin, PID: 8333) which indeed shows Ly α emission (Figure E1). We note that the STIS and our COS pointings are offset by ~ 2 arcsec (~ 168 pc), which indicates that the region emitting Ly α is not entirely overlapping with that emitting ionized carbon, and lies at the outskirts of Pox 186 probably because of Ly α escaping due to the concentrated feedback from the star-formation (Heckman et al. 2011). Only a deep spatial map of Ly α can help identify any potential Ly α emission within Pox 186. Moreover, a statistically significant sample of galaxies such as Pox 186 is required to establish any spatial offset between Ly α emission and carbon emission. Such spatial offsets (~ 168 pc) between Ly α emission and C III] or C IV emission may not be probeable/distinguishable within the reionization era galaxies, simply because of the angular resolution of the existing instruments. So, even if originating from different regions of galaxies, UV carbon emission lines, particularly the stronger C III] line, might still be a good indicator of Ly α emission emerging from the ISM of galaxies even when Ly α is unavailable at redshifts > 6 caused by a significantly large IGM neutral fraction (e.g., Fan et al. 2006).

4.4.2 Lyman Continuum escape fraction

Figure 15 shows C IV/C III] versus EW(C III]) for Pox 186 (red point), along with measurements for galaxies at different redshifts compiled in Schmidt et al. (2021). Schaerer et al. (2022) finds that a C IV/C III] > 0.75 (shaded orange region) is characteristic of strong Lyman Continuum (LyC) leakers, i.e. galaxies with LyC escape fraction $f_{\text{esc}}(\text{LyC}) > 0.1$. Pox 186 exhibits C IV/C III] = 0.30 ± 0.04 , which is much smaller

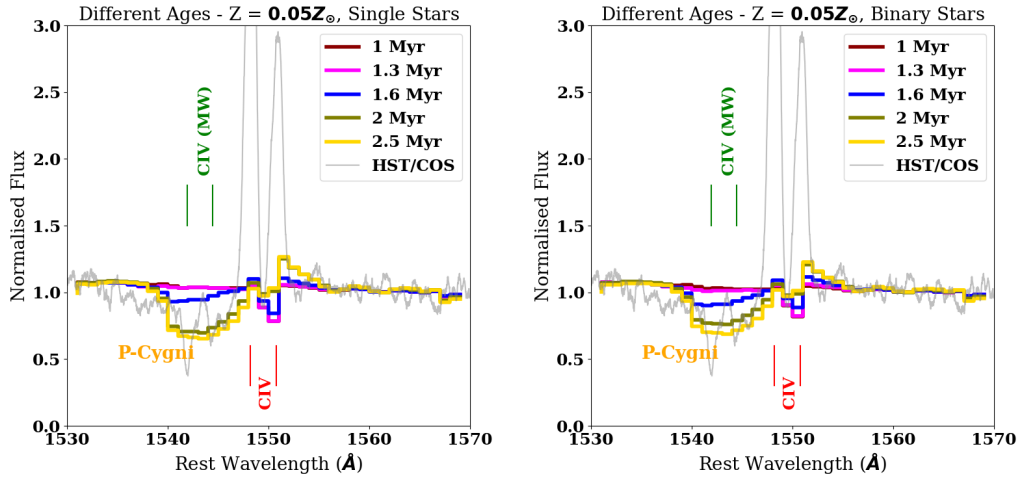


Figure 14. Comparison of observed C IV P-Cygni feature (grey spectrum) within Pox 186 normalized by the continuum level between 1560–1570 Å with the BPASS models at $Z=0.05Z_{\odot}$ comprising single (left-hand panel) and binary stars (right-hand panel) at different ages, i.e., 1 Myr (brown), 1.3 Myr (magenta), 1.6 Myr (blue), 2 Myr (olive) and 2.5 Myr (yellow). The location of C IV emission and absorption from Pox 186 are marked in red. The C IV absorption originating from MW is marked in green.

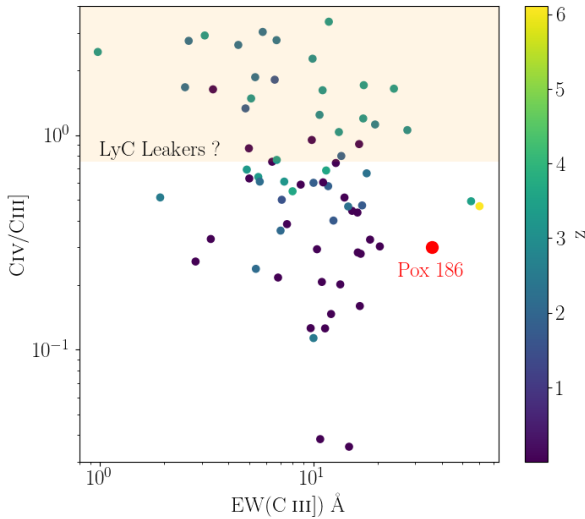


Figure 15. C_{IV}/C_{III} versus $EW(C_{III})$ for Pox 186 (red point) and for published data at different redshifts presented in Schmidt et al. (2021). The orange band represents the $C_{IV}/C_{III} > 0.75$, which is suggested by Schaerer et al. (2022) as strong continuum leakers. Error bars are simply not shown for clarity.

than that exhibited by the strong LyC leakers known so far in the nearby Universe.

Chisholm et al. (2022) suggests that strong LyC leakers have lower values of observed UV continuum slope (β). We estimate $f_{esc}(LyC) \sim 10^{-4}$ from the β slope.

A negligible $f_{esc}(LyC)$ in Pox 186 is consistent with the absence of Ly α for the COS pointing, however, it is inconsistent with an extreme $[O_{III}]_{88\mu m}/[C_{II}]_{157\mu m}$ shown by the Herschel/PACS maps of Pox 186. Katz et al. (2023) demonstrates that $[C_{II}]$ deficit (as in Pox 186) is a good indicator of LyC leakers. We note that the

resolution of the PACS data is much worse ($\geq 9''^4$) than that of our UV and optical data. It is possible that there might be a spatial offset between the region resulting in high $[O_{III}]_{88\mu m}/[C_{II}]_{157\mu m}$ and region emitting bright UV lines.

Izotov et al. (2018) reports an increase in $f_{esc}(LyC)$ with an increase in $[O_{III}]/[O_{II}]$ though with a large scatter. We could not estimate $[O_{III}]/[O_{II}]$ of Pox 186 either at the spatially-resolved data or using the integrated spectrum coinciding with the COS aperture as $[O_{II}]_{\lambda\lambda 3727,3729}$ doublet is undetected. Guseva et al. (2004) present the emission line fluxes of Pox 186 within slits of $1'' \times 3.2''$ and $2'' \times 6''$. Using those line fluxes, we estimate $[O_{III}]/[O_{II}] = 18-22$ for Pox 186 indicating a high $f_{esc}(LyC)$. Moreover, Ramambason et al. (2022) reports a 40% escape fraction of ionizing photons for Pox 186 by using a suite of IR lines.

Figure 15 also shows a couple of reionization era galaxies which have C_{IV}/C_{III} below the threshold proposed by Schaerer et al. (2022), and close to Pox 186. This raises two questions: (1) Is C_{IV}/C_{III} or β slope a good enough predictor for LyC leakers? (2) Were there EoR galaxies which did not contribute to the reionization of the Universe? Such questions can be addressed by making the simultaneous use of UV and FIR observations of large samples of EoR galaxies as well as their local analogues. It would be crucial to do follow-up UV+optical observations via JWST of EoR galaxies, which show extreme IR properties via ALMA, and vice versa.

5 SUMMARY

We investigate the ionized carbon within a local dwarf galaxy Pox 186 using the HST/COS UV data complemented by the GMOS-IFU optical data and Herschel FIR data. Our main results are summarized as follows:

- (i) Using the HST/COS UV emission lines, we measure a redshift

⁴ For reference, the beam size of PACS spectrometer is $\sim 9''$ and $12''$ at 60 μm and 150 μm , respectively.

$z = 0.0040705 \pm 0.000013$ for Pox 186. This corresponds to a luminosity distance of 17.5 Mpc assuming a flat Λ CDM cosmology or 12.6 Mpc assuming Cosmicflows-3.

(ii) The COS/UV data reveals very high EW of carbon emission lines, i.e. $EW(C\text{ III])} = 35.85 \pm 0.73 \text{ \AA}$ and $EW(C\text{ IV}) = 7.75 \pm 0.28 \text{ \AA}$.

(iii) We explore several scenarios to explore the high EW of carbon lines, including a high effective temperature, higher than average carbon-to-oxygen ratio for a given gas-phase metallicity, photoionization CLOUDY models including binary stars, top-heavy IMF and nebular α/Fe enhancement and in-homogeneous dust-distribution. The photoionization models could not simultaneously reproduce all the observables irrespective of dust-reddening, which could be due to the simplistic assumptions of the model parameters.

(iv) The C III] and C IV lines also show broadening with respect to the O III] emission lines though the cause of this broadening remains unknown. We rule out outflows causing broad carbon emission lines as no outflow signatures are found in the velocity profiles of O III] and Si II lines.

(v) Optical integrated spectrum coinciding with COS aperture, shows a broad and faint underlying component in $H\alpha$ along with a narrow component. Ruling out outflows on the basis of UV data, the $H\alpha$ velocity profile indicates a turbulent ISM.

(vi) The C IV doublet shows clearly distinct double peaks for each of the two emission lines, which can be explained via two scenarios, such as pure emission with no absorbing foreground ISM or nebular emission along with a little absorbing ISM in the foreground.

(vii) The high $EW(C\text{ III])}$ and $\log \mathcal{U} = -2.4 \pm 0.4$ suggests a high $EW(Ly\alpha)$ for Pox 186; however, COS spectra do not show any signature of $Ly\alpha$ though a spatially-offset STIS spectrum does show $Ly\alpha$ emission.

(viii) We report an observed UV continuum slope $\beta = -0.36 \pm 0.04$ which corresponds to $f_{\text{esc}}(LyC) \sim 10^{-4}$, indicating that Pox 186 is not a LyC leaker. $C\text{ IV}/C\text{ III]}$ is also below the threshold for LyC leakers suggested by Schaerer et al. (2022). This is in contrast with the extreme $[O\text{ III]}/[C\text{ II}]$ FIR line ratio, 40% escape fraction (Ramambason et al. 2022) and the high $[O\text{ III]}/[O\text{ II}]$ values from the literature. This raises questions on the potential use of β or $C\text{ IV}/C\text{ III]}$ as tracers of LyC leakers.

This work shows that the extreme IR $[O\text{ III]}/[C\text{ II}]$ emission line ratios could correspond to extreme UV properties such as high EW of carbon lines (C III] and C IV), high carbon-to-oxygen ratio, broadened emission carbon line profiles and double-peak within the resonant carbon line doublet, C IV. However, the apparent absence of $Ly\alpha$ emission and negligible LyC escape fraction (as estimated from UV slope and $C\text{ IV}/C\text{ III]}$ ratio) within a dwarf galaxy with such extreme UV and IR properties are puzzling. This requires a similar investigation on a larger sample of similar galaxies with UV+FIR data. The combination of HST and Herschel data for the local Universe, and JWST and ALMA for the reionization era Universe are crucial in carrying out such studies and understanding the similarities and differences between the EoR galaxies and their local analogues.

ACKNOWLEDGEMENTS

NK thanks Joe Hunkeler for their help in setting up the new Gemini IRAF reduction pipeline and debugging the issues with the pipeline. NK thanks Elizabeth Stanway for clarifying information on BPASS models. RS acknowledges financial support from the UK Science and Technology Facilities Council (STFC). JW acknowledges support from the ERC Advanced Grant 695671, “QUENCH”, and the Fondation MERAC. This research is based on observations made

with the NASA/ESA Hubble Space Telescope obtained from the Space Telescope Science Institute, which is operated by the Association of Universities for Research in Astronomy, Inc., under NASA contract NAS 5–26555. These observations are associated with programs GO 16071 and 16445.

This work is further partially based on observations obtained at the Gemini Observatory, which is operated by the Association of Universities for Research in Astronomy, Inc., under a cooperative agreement with the NSF on behalf of the Gemini partnership: the National Science Foundation (United States), the Science and Technology Facilities Council (United Kingdom), the National Research Council (Canada), CONICYT (Chile), the Australian Research Council (Australia), Ministério da Ciência e Tecnologia (Brazil) and SECYT (Argentina)

This research has made use of NASA’s Astrophysics Data System Bibliographic Services; SAOImage DS9, developed by Smithsonian Astrophysical Observatory; Astropy, a community-developed core PYTHON package for Astronomy (Astropy Collaboration et al. 2013); matplotlib (Hunter 2007) and numpy (Harris et al. 2020; Van Der Walt et al. 2011).

This research has made use of the Spanish Virtual Observatory (<https://svo.cab.inta-csic.es>) project funded by MCIN/AEI/10.13039/501100011033/ through grant PID2020-112949GB-I00.

DATA AVAILABILITY

The data presented in this paper are available in the Multimission Archive at the Space Telescope Science Institute (MAST) and Gemini Observatory Archive.

REFERENCES

- Allington-Smith J., et al., 2002, *PASP*, 114, 892
 Arellano-Córdova K. Z., et al., 2022, *ApJ*, 940, L23
 Asplund M., Grevesse N., Sauval A. J., Scott P., 2009, *ARA&A*, 47, 481
 Baldwin J. A., Phillips M. M., Terlevich R., 1981, *PASP*, 93, 5
 Begum A., Chengalur J. N., 2005, *MNRAS*, 362, 609
 Berg D. A., Skillman E. D., Henry R. B. C., Erb D. K., Carigi L., 2016, *ApJ*, 827, 126
 Berg D. A., Chisholm J., Erb D. K., Pogge R., Henry A., Olivier G. M., 2019, *ApJ*, 878, L3
 Best P. N., Röttgering H. J. A., Longair M. S., 2000, *MNRAS*, 311, 1
 Bouwens R. J., et al., 2022, *ApJ*, 931, 160
 Brinchmann J., Kunth D., Durret F., 2008, *A&A*, 485, 657
 Bunker A. J., et al., 2023, *arXiv e-prints*, p. arXiv:2306.02467
 Calzetti D., Kinney A. L., Storchi-Bergmann T., 1994, *ApJ*, 429, 582
 Cardamone C., et al., 2009, *MNRAS*, 399, 1191
 Carniani S., et al., 2017, *A&A*, 605, A42
 Chen Y., et al., 2023, *Nature Astronomy*,
 Chevance M., et al., 2016, *A&A*, 590, A36
 Chisholm J., et al., 2022, *arXiv e-prints*, p. arXiv:2207.05771
 Cooke R., Pettini M., Steidel C. C., Rudie G. C., Nissen P. E., 2011, *MNRAS*, 417, 1534
 Corbin M. R., Vacca W. D., 2002, *ApJ*, 581, 1039
 Cormier D., et al., 2015, *A&A*, 578, A53
 Curtis-Lake E., et al., 2022, *arXiv e-prints*, p. arXiv:2212.04568
 Dinerstein H. L., Lester D. F., Werner M. W., 1985, *ApJ*, 291, 561
 Eggen N. R., Scarlata C., Skillman E., Jaskot A., 2021, *ApJ*, 912, 12
 Eldridge J. J., Stanway E. R., Xiao L., McClelland L. A. S., Taylor G., Ng M., Greis S. M. L., Bray J. C., 2017, *Publ. Astron. Soc. Australia*, 34, e058
 Eldridge J. J., Beasar E. R., Britavskiy N., 2020, *MNRAS*, 495, L102

- Erb D. K., Pettini M., Shapley A. E., Steidel C. C., Law D. R., Reddy N. A., 2010, *ApJ*, **719**, 1168
- Fan X., Carilli C. L., Keating B., 2006, *ARA&A*, **44**, 415
- Feltre A., Charlot S., Gutkin J., 2016, *MNRAS*, **456**, 3354
- Garnett D. R., Skillman E. D., Dufour R. J., Peimbert M., Torres-Peimbert S., Terlevich R., Terlevich E., Shields G. A., 1995, *ApJ*, **443**, 64
- Giavalisco M., et al., 2004, *ApJ*, **600**, L93
- Gordon K. D., Clayton G. C., Misselt K. A., Landolt A. U., Wolff M. J., 2003, *ApJ*, **594**, 279
- Grogin N. A., et al., 2011, *ApJS*, **197**, 35
- Guseva N. G., Papaderos P., Izotov Y. I., Noeske K. G., Fricke K. J., 2004, *A&A*, **421**, 519
- Harris C. R., et al., 2020, *Nature*, **585**, 357
- Hashimoto T., et al., 2019, *PASJ*, **71**, 71
- Heckman T. M., et al., 2011, *ApJ*, **730**, 5
- Hook I. M., Jørgensen I., Allington-Smith J. R., Davies R. L., Metcalfe N., Murowinski R. G., Crampton D., 2004, *PASP*, **116**, 425
- Houck J. R., et al., 2004, *ApJS*, **154**, 211
- Hunter J. D., 2007, *Computing in Science & Engineering*, **9**, 90
- Hutchison T. A., et al., 2019, *ApJ*, **879**, 70
- Illingworth G. D., et al., 2013, *ApJS*, **209**, 6
- Izotov Y. I., Wöröck G., Schaerer D., Guseva N. G., Thuan T. X., Fricke K. J., Verhamme A., Orlitová I., 2018, *MNRAS*, **478**, 4851
- Jiang L., et al., 2021, *Nature Astronomy*, **5**, 256
- Katz H., et al., 2023, *MNRAS*, **518**, 270
- Kauffmann G., et al., 2003, *MNRAS*, **346**, 1055
- Kewley L. J., Dopita M. A., Sutherland R. S., Heisler C. A., Trevena J., 2001, *ApJ*, **556**, 121
- Kewley L. J., Nicholls D. C., Sutherland R. S., 2019, *ARA&A*, **57**, 511
- Kniazev A. Y., Grebel E. K., Hao L., Strauss M. A., Brinkmann J., Fukugita M., 2003, *ApJ*, **593**, L73
- Koekemoer A. M., et al., 2011, *ApJS*, **197**, 36
- Kourkchi E., Courtois H. M., Graziani R., Hoffman Y., Pomarède D., Shaya E. J., Tully R. B., 2020, *AJ*, **159**, 67
- Kumari N., 2018, PhD thesis, University of Cambridge, UK
- Kumari N., James B. L., Irwin M. J., 2017, *MNRAS*, **470**, 4618
- Kumari N., James B. L., Irwin M. J., Amorín R., Pérez-Montero E., 2018, preprint, ([arXiv:1802.04797](https://arxiv.org/abs/1802.04797))
- Kumari N., James B. L., Irwin M. J., Aloisi A., 2019, *MNRAS*, **485**, 1103
- Kumari N., Amorín R., Pérez-Montero E., Vílchez J., Maiolino R., 2021, *MNRAS*, **508**, 1084
- Kunth D., Joubert M., 1985, *A&A*, **142**, 411
- Kunth D., Sargent W. L. W., Kowal C., 1981, *A&AS*, **44**, 229
- Laigle C., et al., 2016, *ApJS*, **224**, 24
- Le Fèvre O., et al., 2019, *A&A*, **625**, A51
- Leitherer C., Leão J. R. S., Heckman T. M., Lennon D. J., Pettini M., Robert C., 2001, *ApJ*, **550**, 724
- Leitherer C., Ortiz Otlávaro P. A., Bresolin F., Kudritzki R.-P., Lo Faro B., Pauldrach A. W. A., Pettini M., Rix S. A., 2010, *ApJS*, **189**, 309
- Leitherer C., Tremonti C. A., Heckman T. M., Calzetti D., 2011, *AJ*, **141**, 37
- Madden S. C., et al., 2013, *PASP*, **125**, 600
- Mainali R., et al., 2020, *MNRAS*, **494**, 719
- Maiolino R., et al., 2015, *MNRAS*, **452**, 54
- Maseda M. V., et al., 2017, *A&A*, **608**, A4
- Nakajima K., Ouchi M., 2014, *MNRAS*, **442**, 900
- Nakajima K., et al., 2018, *A&A*, **612**, A94
- Newville M., Stensitzki T., Allen D. B., Ingargiola A., 2014, LMFIT: Non-Linear Least-Square Minimization and Curve-Fitting for Python, Zenodo, [doi:10.5281/zenodo.11813](https://doi.org/10.5281/zenodo.11813)
- Nicholls D. C., Sutherland R. S., Dopita M. A., Kewley L. J., Groves B. A., 2017, *MNRAS*, **466**, 4403
- Pérez-Montero E., 2017, *PASP*, **129**, 043001
- Pérez-Montero E., Vílchez J. M., 2009, *MNRAS*, **400**, 1721
- Pérez-Montero E., García-Benito R., Vílchez J. M., 2019, *MNRAS*, **483**, 3322
- Polles F. L., et al., 2019, *A&A*, **622**, A119
- Ramambason L., et al., 2022, *A&A*, **667**, A35
- Reddy N. A., et al., 2018, *ApJ*, **853**, 56
- Ren Y. W., et al., 2023, *ApJ*, **945**, 69
- Rigby J. R., Bayliss M. B., Gladders M. D., Sharon K., Wuyts E., Dahle H., Johnson T., Peña-Guerrero M., 2015, *ApJ*, **814**, L6
- Robertson B. E., 2021, arXiv e-prints, [p. arXiv:2110.13160](https://arxiv.org/abs/2110.13160)
- Robertson B. E., Ellis R. S., Dunlop J. S., McLure R. J., Stark D. P., 2010, *Nature*, **468**, 49
- Rodrigo C., Solano E., 2020, in XIV.0 Scientific Meeting (virtual) of the Spanish Astronomical Society. p. 182
- Rodrigo C., Solano E., Bayo A., 2012, SVO Filter Profile Service Version 1.0, IVOA Working Draft 15 October 2012, [doi:10.5479/ADS/bib/2012ivoa.rept.1015R](https://doi.org/10.5479/ADS/bib/2012ivoa.rept.1015R)
- Schaerer D., Contini T., Pindao M., 1999, *A&AS*, **136**, 35
- Schaerer D., et al., 2022, *A&A*, **658**, L11
- Schlafly E. F., Finkbeiner D. P., 2011, *ApJ*, **737**, 103
- Schmidt K. B., et al., 2021, *A&A*, **654**, A80
- Searle L., Sargent W. L. W., 1972, *ApJ*, **173**, 25
- Senchyna P., et al., 2017, *MNRAS*, **472**, 2608
- Senchyna P., Stark D. P., Chevallard J., Charlot S., Jones T., Vidal-García A., 2019, *MNRAS*, **488**, 3492
- Shapley A. E., Steidel C. C., Pettini M., Adelberger K. L., 2003, *ApJ*, **588**, 65
- Smit R., et al., 2018, *Nature*, **553**, 178
- Sobral D., Matthee J., Darvish B., Schaerer D., Mobasher B., Röttgering H. J. A., Santos S., Hemmati S., 2015, *ApJ*, **808**, 139
- Stark D. P., 2016, *ARA&A*, **54**, 761
- Stark D. P., et al., 2014, *MNRAS*, **445**, 3200
- Stark D. P., et al., 2017, *MNRAS*, **464**, 469
- Tang M., Stark D. P., Chevallard J., Charlot S., Endsley R., Congiu E., 2021, *MNRAS*, **501**, 3238
- Topping M. W., Shapley A. E., Stark D. P., Endsley R., Robertson B., Greene J. E., Furlanetto S. R., Tang M., 2021, *ApJ*, **917**, L36
- Van Der Walt S., Colbert S. C., Varoquaux G., 2011, *Computing in Science & Engineering*, **13**, 22
- Vanzella E., et al., 2016, *ApJ*, **821**, L27
- Vanzella E., et al., 2017, *ApJ*, **842**, 47
- Veilleux S., Osterbrock D. E., 1987, *ApJS*, **63**, 295
- Vílchez J. M., Pagel B. E. J., 1988, *MNRAS*, **231**, 257
- Witstok J., et al., 2022, *MNRAS*, **515**, 1751
- Yang H., Malhotra S., Rhoads J. E., Wang J., 2017, *ApJ*, **847**, 38
- van Dokkum P. G., 2001, *PASP*, **113**, 1420

APPENDIX A: TARGET ACQUISITION IMAGE

Figure A1 shows one of the two NUV target acquisition images taken with taking the spectroscopic COS observations.

APPENDIX B: OPTICAL FLUX SCALING AND SYSTEMATIC UNCERTAINTIES

Note that the flux calibration obtained from the spectrophotometric standard star is relative and not absolute. To determine the optical emission line fluxes accurately, we follow the procedure described below. We first compare the ground-based Gemini/optical spectroscopic fluxes with the space-based archival HST imaging taken with the F658N filter. To do so, we extract the flux within an aperture of 1.25'' radius (matching the COS aperture) on the WFC3/F658N image, subtract a background and apply the aperture correction. This value is then multiplied with the inverse sensitivity and the FWHM of the filter (estimated from synthetic photometry package `SYNPHOT`) to get the total flux within the aperture in the cgs units. We note that the width of an HST/WFC3 filter can be defined in several ways; however, we chose to use FWHM following the methodology of Laigle et al. (2016) for generating large photometric catalogues. To get the WFC3/F658N equivalent from Gemini optical data, we multiply the COS-matched Gemini spectrum with the transmission curve of the

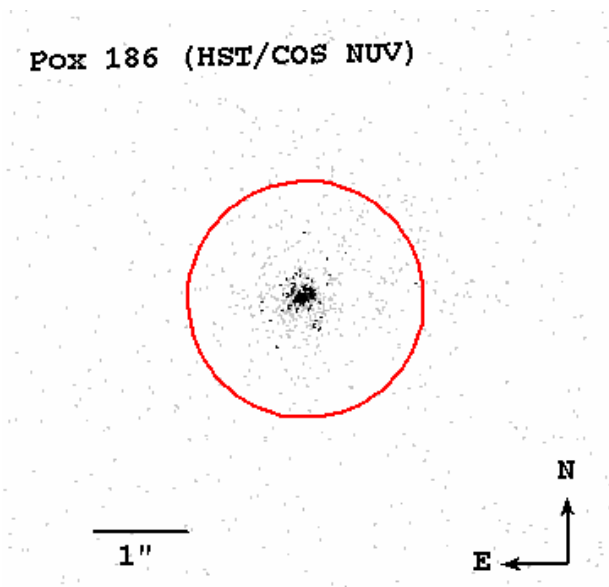


Figure A1. HST/COS NUV target acquisition image of Pox 186. The red circle denotes the 2.5 arcsec COS spectroscopic aperture and is centered at (RA, Dec): (13 25 48.641, -11 36 37.94). The compass on the bottom-right of the figure shows North and East on the HST image. At the luminosity distance of this galaxy (i.e. 17.5Mpc), 1 arcsec corresponds to 84 pc.

WFC3/F658N filter available from the SVO Filter Profile Service (Rodrigo et al. 2012; Rodrigo & Solano 2020). We integrate the resultant spectrum to get the HST equivalent of Gemini flux. This gives us a scaling factor of ~ 2.7 for the Gemini spectra taken with R831 grating at $\sim 6900\text{\AA}$.

Note that we have three sets of Gemini spectra taken B600 grating at $\sim 4650\text{\AA}$ and R831 grating at 6900\AA and 8900\AA . The Gemini spectra taken with B600/4650 \AA and R831/8900 \AA could in principle be scaled with respect to the scaled Gemini spectra taken with R831/6900 \AA , however, the continuum is too faint to do such an exercise. So, we estimate the $E(B-V)$ from the unscaled $H\gamma/H\beta$ ratio from the B600/4650 \AA , and then use it with the scaled H α line flux to estimate the scaling factor for H β and hence the corresponding spectra. A similar procedure based on $E(B-V)$ is followed where we predict the H I P10 line flux obtained from the R831/8900 \AA spectra, thus determining the scaling factor of these spectra.

These scaling factors give us H β flux value in reasonable agreement with that derived by Guseva et al. (2004) for different-sized slits.

To determine the systematic uncertainties on flux calibration, we compare the integrated Gemini/IFU spectra of the standard photometric star (HZ44) with that available from CALSPEC, which gives us a systematic uncertainty of 50%.

APPENDIX C: OPTICAL EMISSION LINE FLUX MAPS

Figures C1 and C3 show the emission line flux maps obtained by fitting a single Gaussian to each optical line. The orientation of the FOV is different in the two figures because each set of Figures here is obtained from different observing programs with different position angle (see Figure 2). A compass is shown in each figure to show the orientation. Figures C2 show the maps of optical emission line ratios used in the classical emission line ratio diagrams (or the so-called BPT diagrams).

APPENDIX D: BPASS MODELS RESULTS WITH IMF SLOPE -2.35 AND WITHOUT α /FE ENHANCEMENT

We explore whether the extreme radiation field from the stellar population could cause the high EW of carbon lines by using the BPASS models without α /Fe enhancement. Figure D1 shows BPASS models (version 2.2.1, upper IMF slope of -2.35 and upper mass limit of $300 M_{\odot}$) consisting of single stars at stellar metallicity of $0.05 Z_{\odot}$ and age of ~ 1 Myr are able to reproduce observed EW(C IV) for $\log U = -1.5$ and any value of hydrogen density (n_H). However, the same BPASS model consisting of binary stars is able to produce the observed EW(C IV) only for hydrogen density $\log n_H/\text{cm}^{-3} = 3$.

Since EW(C IV $\lambda\lambda$ 1548,1550) for Pox 186 is reproduced by the BPASS models with a particular set of physical parameters, we use the same BPASS models to explore whether stellar populations radiation field from the stellar population could produce the high EW(C III]). However, neither single nor binary stars are sufficient to achieve such a high value of EW(C III]) exhibited by Pox 186 (Figure D2). Hence we discard the possibility that the extreme radiation field from the stellar population is responsible for the high EW of carbon lines.

APPENDIX E: Ly α EMISSION WITHIN HST/STIS SPECTRUM

Figure E1 shows a noisy yet prominent Ly α emission in the UV spectrum of Pox 186 taken with Space Telescope Imaging Spectrograph (onboard HST) using the G140L grating. The aperture used for taking observation was 52×0.5 , which corresponds to a slit of 0.5 arcsecs, and was centred at RA and Dec of 13 25 48.50 and -11 36 37.70, respectively. This translates into a spatial offset of 2 arcsecs between the STIS and our COS pointings.

This paper has been typeset from a $\text{\TeX}/\text{\LaTeX}$ file prepared by the author.

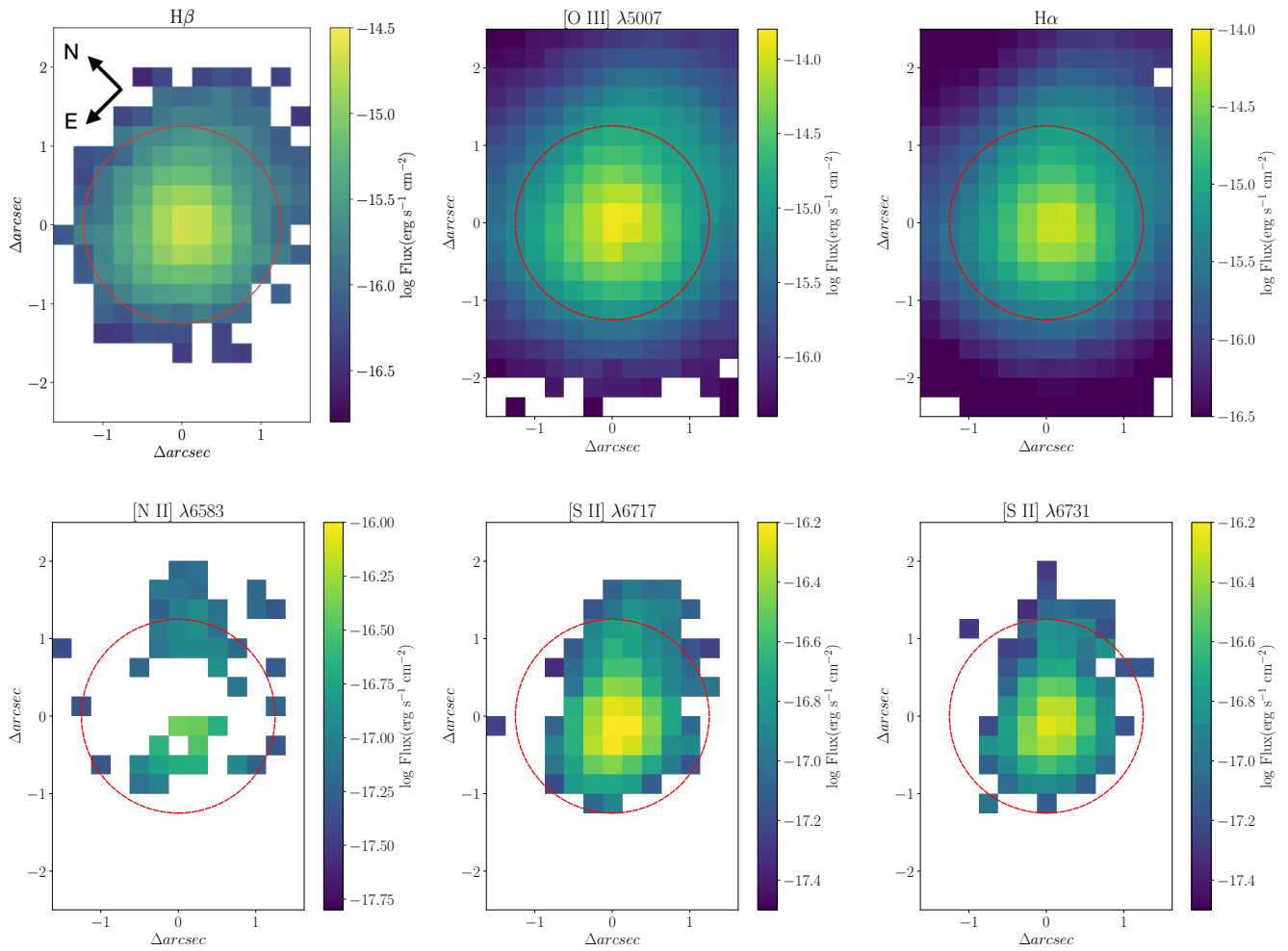


Figure C1. Optical emission line flux maps of Pox186 obtained from GMOS-N IFU taken as part of program GN-2020A-FT-105. The orientation of the maps is indicated by the compass on the $H\beta$ flux map. The white pixels indicate the regions where $S/N < 3$. The red circle indicates the location of COS aperture.

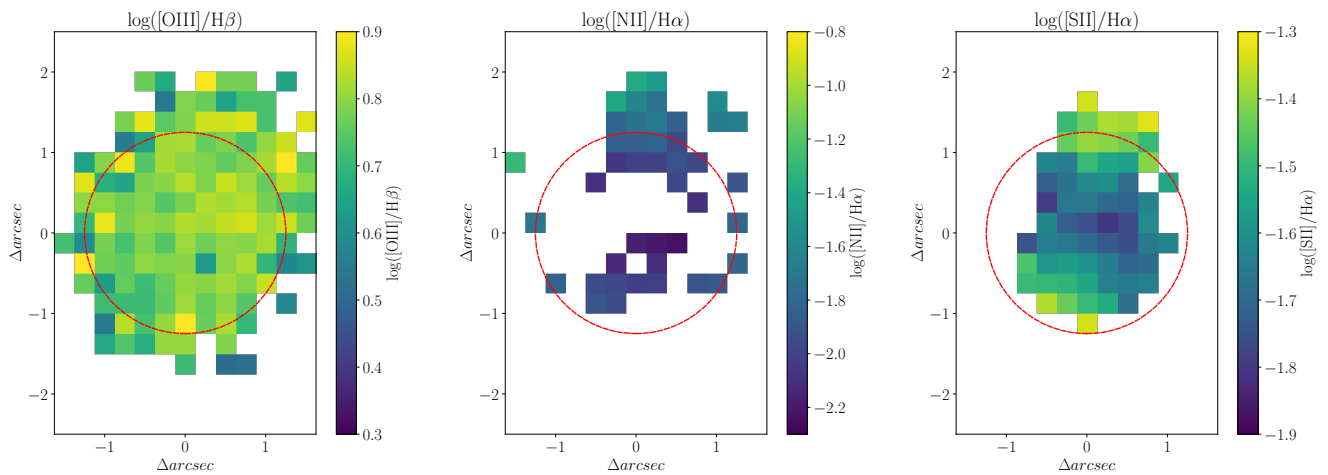


Figure C2. Maps of the optical emission line ratios created from using the flux maps shown in Figure C1: $[O\ III]/H\beta$ (left-hand panel), $[N\ II]/H\alpha$ (middle panel) and $[S\ II]/H\alpha$ (right-hand panel). The white pixels indicate the regions where $S/N < 3$. The red circle indicates the location of COS aperture.

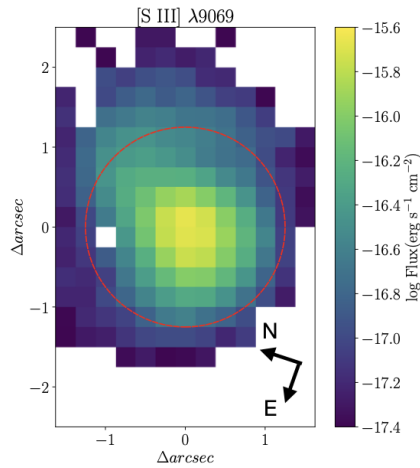


Figure C3. [S III] λ 9069 emission line flux map obtained from GMOS-N IFU data taken as part of the program GN-2021-FT-111. The orientation of the map is indicated by the compass on the lower-left corner. The white pixels indicate the regions where $S/N < 3$. The red circle indicates the location of COS aperture.

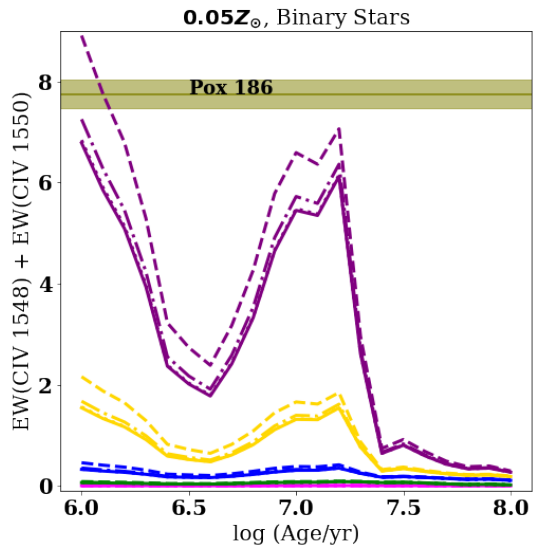
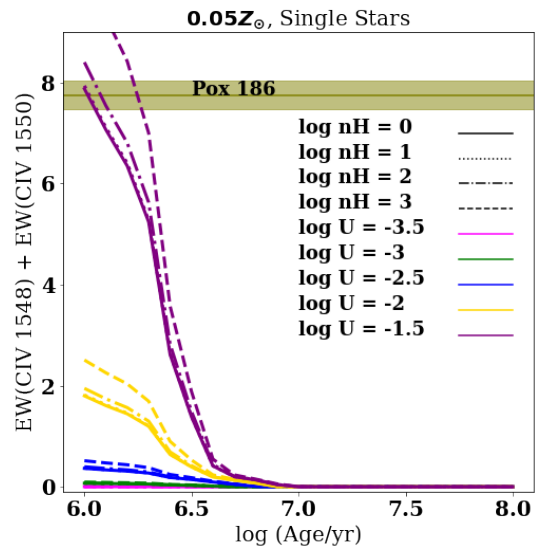


Figure D1. BPASS models showing the variation of the equivalent width of C IV emission lines for single stars (upper panel) and binary stars (lower panel), and for a metallicity of $0.05Z_{\odot}$. Note that we also produced similar plots for other metallicities but a metallicity of $0.05Z_{\odot}$ could only reproduce the $EW(C IV)$ as demonstrated in the lower panel. Five values of $\log \mathcal{U}$ are considered i.e., -1.5 (purple), -2.0 (yellow), -2.5 (blue), -3.0 (green), -3.5 (magenta). Similarly, we consider four values of hydrogen densities, $\log n_H$, i.e., 0 (solid curve), 1 (dotted curve), 2 (dash-dot curve), 3 (dashed curve). The observed EW of C III] and (upper panel) C IV (lower) and the associated uncertainties are represented by the solid horizontal black line and the shaded olive green region. Single star models with any n_H , but high $\log \mathcal{U}$ ($=-1.5$) at a low metallicity ($0.05 Z_{\odot}$) can reproduce the observed $EW(C IV)$ at ages of $\log(\text{Age}/\text{yr}) = 6-6.5$. However, when binary stars are considered, very high hydrogen density ($\log n_H = 3$), high ionization parameter ($\log \mathcal{U} = -1.5$) and low metallicity ($0.05 Z_{\odot}$) are required to reproduce the observed $EW(C IV)$ at ages of $\log(\text{Age}/\text{yr}) \sim 6.25$.

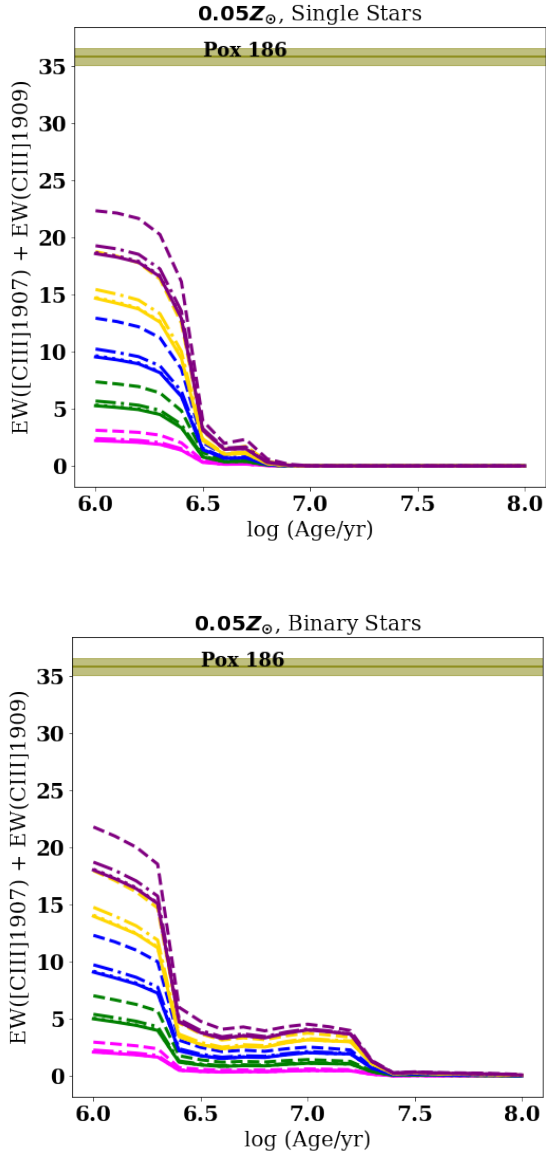


Figure D2. BPASS models showing the variation of the equivalent width of the C III] emission lines for single stars (upper panel) and binary stars (lower panel), and for a metallicity of $0.05Z_{\odot}$. Five values of $\log \mathcal{U}$ are considered i.e., -1.5 (purple), -2.0 (yellow), -2.5 (blue), -3.0 (green), -3.5 (magenta). Similarly, we consider four values of hydrogen densities, $\log n_H$, i.e., 0 (solid curve), 1 (dotted curve), 2 (dashdot curve), 3 (dashed curve). The observed EW of C III] and the associated uncertainties are represented by the solid horizontal black line and the shaded olive green region. The models sufficient to produce high C IV are insufficient to reproduce the high C III].

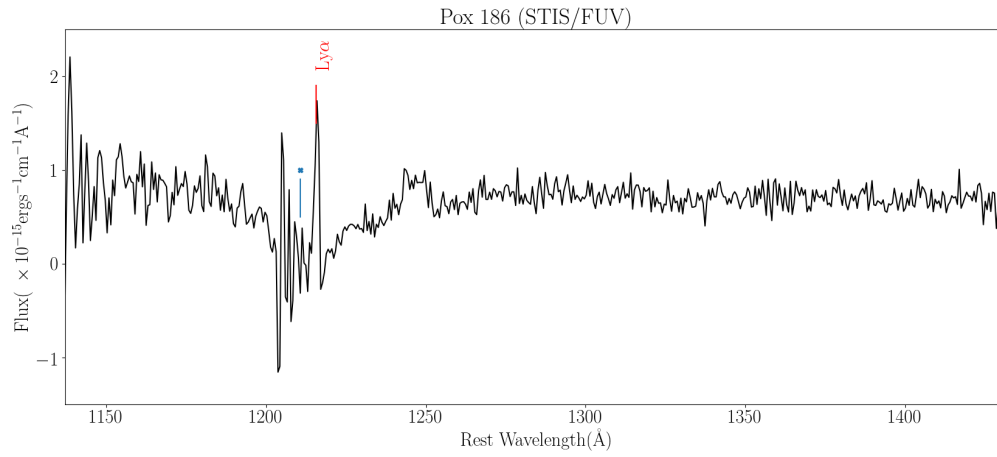


Figure E1. A noisy yet prominent Ly α emission amidst the damped Ly α absorption is detected within the STIS/FUV spectrum of Pox 186. The blue cross shows the location of geocoronal emission.